

Moving Mesh with Streamline Upwind Petrov-Galerkin (MM-SUPG) Method for Time-dependent Convection-Dominated Convection-Diffusion Problems

Xianping Li*

Matthew McCoy†

Time-dependent convection-diffusion problems is considered, particularly when the diffusivity is very small and sharp layers exist in the solutions. Nonphysical oscillations may occur in the numerical solutions when using regular mesh with standard computational methods. In this work, we develop a moving mesh SUPG (MM-SUPG) method, which integrates the streamline upwind Petrov-Galerkin (SUPG) method with the moving mesh partial differential equation (MMPDE) approach. The proposed method is designed to handle both isotropic and anisotropic diffusivity tensors. For the isotropic case, we focus on improving the stability of the numerical solution by utilizing both artificial diffusion from SUPG and mesh adaptation from MMPDE. And for the anisotropic case, we focus on the positivity of the numerical solution. We introduce a weighted diffusion tensor and develop a new metric tensor to control the mesh movement. We also develop conditions for time step size so that the numerical solution satisfies the discrete maximum principle (DMP). Numerical results demonstrate that the proposed MM-SUPG method provides results better than SUPG with fixed mesh or moving mesh without SUPG.

1 Introduction

We consider the time-dependent convection-diffusion equation defined over the time-independent domain $\Omega \subset \mathbb{R}^2$ with a Lipschitz boundary and denote $\Omega_T = \Omega \times [0, T]$. The equation is given by:

$$u_t - \varepsilon \nabla \cdot (\mathbb{D} \nabla u) + \mathbf{b}(\mathbf{x}) \cdot \nabla u = f(\mathbf{x}, t) \quad \text{in} \quad \Omega \times (0, T] \quad (1a)$$

$$u(\mathbf{x}, t) = g(\mathbf{x}, t), \quad \text{on} \quad \partial\Omega \times [0, T] \quad (1b)$$

$$u(\mathbf{x}, 0) = u_0(\mathbf{x}), \quad \text{in} \quad \Omega \times \{t = 0\}. \quad (1c)$$

*College of Integrative Sciences and Arts, Arizona State University, AZ, 85212, USA (xianping@asu.edu)

†Kansas City, MO, 64157, USA (matthewmccoy6@gmail.com)

Here, $\mathbb{D} = \mathbb{D}(\mathbf{x})$ on $\Omega_T = \Omega \times (0, T]$ is the diffusivity tensor that is symmetric and positive-definite (SPD), \mathbf{b} represents an incompressible velocity field, while g , u_0 , and f are sufficiently smooth functions. The parameter $\varepsilon \in (0, 1]$ is the scaling factor for the diffusivity coefficient. When \mathbb{D} has the same eigenvalues, the problem is isotropic. In the anisotropic case, the eigenvalues of \mathbb{D} are different, which indicates that diffusion in one direction is faster than in the other.

Our focus lies in the convection-dominated scenario where ε is much smaller than $\|\mathbf{b}\|_{L^\infty}$. Such problems arise in various fields, including pollutant dispersal in rivers, atmospheric pollution, the Stefan problem, turbulent transport, and are particularly intriguing in the investigation of the Navier–Stokes equations with large Reynolds numbers, see [1] for relevant applications. When ε is small, non-physical oscillations tend to arise in the solution unless an extremely fine spatial-temporal discretization is employed, incurring substantial computational costs. To enhance stability, artificial diffusion in the direction of \mathbf{b} is proposed in [2] to be added to the standard Galerkin finite element method.

The streamline upwind Petrov-Galerkin (SUPG) method has proven to be particularly effective in numerically addressing boundary and interior layer problems in both time-dependent and time-independent scenarios [3, 4, 5, 6]. The motivation behind SUPG is to employ upwinding of the test functions along the streamlines, aiming to enhance the diffusion of solution. This concept is most clearly illustrated in the 1D time-independent case using finite difference stencils:

$$\frac{\partial u}{\partial x} = -\varepsilon \frac{\partial^2 u}{\partial x^2}. \quad (2)$$

When applying the finite difference method with only the center stencil, one obtains a numerical approximation that, depending on ε , tends to be under-diffusive. Conversely, utilizing only an upwind stencil leads to excessive diffusion, known as over-diffusive. As the exact solution typically lies somewhere in between these extremes, it prompts the adoption of upwinding the center scheme [7]. This method was initially proposed by Brooks and Hughes for incompressible Navier-Stokes problems [2], and has since proven to be fruitful in studying those equations [8, 9]. Comparison among different methods for the steady-state form of equation (1) have been performed in [10].

Efforts have been made to numerically solve equation (1a) for time-independent solutions, particularly focusing on steady flows [3, 11], by employing adaptive mesh methods in conjunction with SUPG, especially when $\varepsilon \ll 1$. Notably, mesh adaptation has emerged as a potent tool in addressing convection-dominated problems. Our investigation targets a specific class of problems characterized by two key properties: artificial (non-physical) oscillations and sharp layers, encompassing both interior and boundary layers. Consequently, our interest lies in devising a mesh strategy grounded in anisotropic mesh adaptation techniques.

Several notable methodologies have been explored for solving equation (1). For instance, in [12], Lagrange-Galerkin error analysis demonstrated first-order uniform convergence in ε . Additionally, ε -uniform convergence theory for finite element method with homogeneous boundary conditions was investigated in [13]. Carey et al. introduced adaptive mesh refinement (AMR) in [14], while Chin-chapatnam et al. explored unsymmetric and symmetric meshless collocation techniques with radial basis functions in [15]. Of particular interest are the so-called SOLD (Spurious Oscillations at Layers Diminishing) schemes, which have been extensively studied in [16, 17, 18]. These schemes involve the addition of either isotropic or anisotropic artificial diffusion to the Galerkin formulation. Furthermore, in [19], local discontinuous Galerkin (LDG) methods were employed on a class of layer-adapted Shishkin and Bakhvalov-type meshes, accompanied by error analysis, to approximate equation (1).

For time-dependent problems, Wang et al. utilized the singular boundary method with $f = 0$ in [20], employing an exponential variable transform along with the Fourier transform. Additionally, unfitted finite element methods have gained traction for tackling equation (1) in time-dependent

domains [21]. These types of unfitted FEMs are known by various names such as XFEM, CutFEM, Finite Cell Method, and TraceFEM (refer to the sources in [21] along with [22, 23]). It is worth noting, as mentioned in [24], that unfitted techniques may encounter conditioning difficulties, which are addressed using specialized finite element spaces and aggregation technique.

In all the above mentioned methods, only isotropic diffusivity tensors were considered. However, in many practical applications, the diffusivity tensor is anisotropic. When the mesh is not aligned in the principal diffusion direction, non-physical oscillations may occur when using standard computational methods [25]. Special care must be taken to ensure that the numerical solution satisfies the discrete maximum principle (DMP). For problem with only diffusion, metric tensors has been developed in [25] for time-independent problems to adapt the mesh such as $\mathbb{M}_{DMP} = \theta_K \mathbb{D}_K^{-1}$ based on DMP satisfaction and $\mathbb{M}_{DMP+adap} = C_K (\det(\mathbb{D}))^{\frac{1}{d}} \mathbb{D}_K^{-1}$ based on DMP satisfaction as well as minimization of interpolation errors. For time-dependent problems, condition for time step size is also developed in [26] to ensure that the numerical solutions satisfy DMP. Lu et al. investigated the satisfaction of DMP for anisotropic diffusion-convection-advection problems in [27]. However, it is even more challenge for numerical solutions of convection-dominated convection-diffusion problems to satisfy the DMP, which will be addressed in this paper.

In this paper, we propose to integrate the moving mesh partial differential equation (MMPDE) method with streamline upwind Petro-Galerkin (SUPG) method and call it as moving mesh SUPG (MM-SUPG) method. It works for both time-independent and time-dependent flows characterized by initial sharp layers, and can deal with both isotropic and anisotropic diffusivity tensors. It has been observed that, even for isotropic diffusivity, oscillations can persist with adapted meshes [28]. The challenge in numerically solving equation (1) becomes evident particularly when $\varepsilon \ll 1$ and the initial profile experiences convection over time or when the profile features sharp regular, parabolic, corner, or interior layers that develop or exist initially. Meanwhile, when \mathbb{D} is anisotropic, non-physical solutions may appear in the numerical solution, which is a violation of DMP [25, 26]. To address this issue, we introduce a metric tensor to control the mesh movement and develop conditions for mesh and time step size so that the numerical solution satisfies DMP.

The remainder of this paper is organized as follows. In Section 2, we give a brief introduction for SUPG and MMPDE, and propose our MM-SUPG method. Section 3 presents numerical examples for isotropic diffusivity case to demonstrate the effectiveness of our approach, while also delineating the constraints of the moving mesh method. In Section 4, we investigate the satisfaction of discrete maximum principle for anisotropic diffusion. Finally, a summary and some conclusions are presented in Section 5.

2 Moving Mesh with Streamline Upwind Petrov-Galerkin (MM-SUPG) Method

Firstly, we give a brief introduction to SUPG method and MMPDE method. Then we explain in details our MM-SUPG method, the integration of MMPDE with SUPG.

2.1 SUPG method

Consider the convection-diffusion equation (1a) with homogeneous Dirichlet boundary conditions (1b) and initial condition (1c). The SUPG method is a stabilized finite element method that introduces artificial diffusion to the Galerkin formulation. Let $L^2(\Omega)$ and $H^k(\Omega)$, $k \geq 1$ denote the standard Lebesgue and Sobolev spaces, respectively. Let $H_g^1(\Omega) = \{v \in H^1(\Omega), v|_{\partial\Omega} = g\}$ and $H_0^1(\Omega) = \{v \in$

$H^1(\Omega)$, $v|_{\partial\Omega} = 0$. The weak formulation of (1a) is to find $u \in H_g^1(\Omega)$ such that

$$\int_{\Omega} u_t v - \varepsilon \int_{\Omega} \nabla \cdot (\mathbb{D} \nabla u) v + \int_{\Omega} (\mathbf{b} \cdot \nabla u) v = \int_{\Omega} f v, \quad \forall v \in H_0^1(\Omega). \quad (3)$$

We consider an affine family of simplicial triangulations $\{\mathcal{T}_h\}$ for Ω and denote the piecewise linear finite element space as $V^h = (v \in H^1(\Omega), v|_K \in \mathcal{P}_1^K, \forall K \in \mathcal{T}_h)$, where \mathcal{P}_1^K is the linear polynomial space in element K . Denote by $U^h = V^h \cap H_g^1(\Omega)$ and $U_0^h = V_h \cap H_0^1(\Omega)$. The standard Galerkin method is to find $u_h \in U^h$ such that

$$\int_{\Omega} u_t v_h - \varepsilon \int_{\Omega} \nabla \cdot (\mathbb{D} \nabla u_h) v_h + \sum_{K \in \mathcal{T}_h} (\mathbf{b} \cdot \nabla u_h) v_h = \int_{\Omega} f v_h, \quad \forall v_h \in U_0^h. \quad (4)$$

The essential idea of SUPG involves altering the test function space to operate within the realm of functions that upwind the trial functions along the streamlines. This can be represented as the space:

$$U_h^{\text{SUPG}} = \left\{ v_h + \tau_K \mathbf{b} \cdot \nabla v_h \mid v_h \in U_0^h \right\}, \quad (5)$$

where τ_K is the stabilization parameter. Therefore, one may perceive the space U_h^{SUPG} as a suitable stabilized test space for singularly perturbed problems. The weak formulation for SUPG method is given as follows: find $u \in H^1(\Omega)$ such that

$$\int_{\Omega} u_t v_h - \varepsilon \int_{\Omega} \nabla \cdot (\mathbb{D} \nabla u_h) (v_h + \tau_K \mathbf{b} \cdot \nabla v_h) + \sum_{K \in \mathcal{T}_h} (\mathbf{b} \cdot \nabla u_h) (v_h + \tau_K \mathbf{b} \cdot \nabla v_h) = \int_{\Omega} f (v_h + \tau_K \mathbf{b} \cdot \nabla v_h), \quad \forall v_h \in U_0^h. \quad (6)$$

A conventional choice of τ_K on mesh \mathcal{T}_h is

$$\tau_{\mathcal{T}_h}^K = \begin{cases} c_0 \text{diam}(K) \tau_h & \text{if } \text{Pe}_K > 1 \text{ convection-dominated} \\ c_1 \text{diam}(K) \tau_h^2 & \text{if } \text{Pe}_K \leq 1 \text{ diffusion-dominated} \end{cases}, \quad (7)$$

where Pe_K denotes the element-wise Péclet number given by

$$\text{Pe}_K = \frac{\|\mathbf{b}\|_{\infty} \text{diam}(K) \tau_h}{2\varepsilon}. \quad (8)$$

It determines local convection-dominated or diffusion-dominated regimes on the current mesh \mathcal{T}_K . There is flexibility in defining $\text{diam}(K) \tau_h$ and in selecting c_0 and c_1 . This paper primarily focuses on scenarios where Pe_K is large with respect to $\varepsilon^{-1} \|\mathbf{b}\|_{\infty}$. Typically, individual bilinear forms in the SUPG formulation are estimated, and $\tau_{\mathcal{T}_h}^K$ is derived based on those errors. In [3], such a method was employed using error estimates in the discrete norm

$$\|w\|_{\varepsilon, k}^2 = \varepsilon \|\nabla w\|^2 + \sum_{K \in \mathcal{T}_K} \tau_{\mathcal{T}_h}^K \|\mathbf{b} \cdot \nabla w\|_{L^2(K)}^2, \quad \forall w \in H_0^1(\Omega) \quad (9)$$

for time independent \mathbf{b} . However, our method relies on different error estimates for defining the metric tensor along with a mesh functional approach. If a source term is introduced, say $c \in L^{\infty}(0, T; L^{\infty}(\Omega))$, it has been proposed that the FE perturbation parameters should consider this source term [29, 30, 31, 32].

In the case of anisotropic mesh adaptation, $\text{diam}(K)_{\mathcal{T}_h}$ will be updated with each new mesh as the elements stretch and shrink. In this paper, we define $\tau_{\mathcal{T}_h}^K$ as

$$\tau_{\mathcal{T}_h}^K = \frac{\text{diam}(K)_{\mathcal{T}_K}}{2\|\mathbf{b}\|_\infty} \xi(\text{Pe}_K), \quad (10)$$

which is based on the stabilization parameter selected in [11]. Common choices of $\text{diam}(K)_{\mathcal{T}_h}$ include the length of the longest edge of the element K projected onto \mathbf{b} and the diameter of K in the direction of \mathbf{b} . In this paper, for each $K \in \mathcal{T}_h$, we define

$$\text{diam}(K) = \sup_{\mathbf{x}_1, \mathbf{x}_2 \in K} \|\mathbf{x}_1 - \mathbf{x}_2\| \quad (11)$$

and

$$\xi(\text{Pe}_K) = \min \left\{ 1, \frac{\text{Pe}_K}{3} \right\}. \quad (12)$$

2.2 Moving mesh partial differential equations (MMPDE)

Moving mesh methods are instrumental in addressing domains where the solution exhibits excessively large gradient, such as sharp layers. Traditional methods like fitted operator methods, finite difference methods, finite element methods with uniform or Shishkin-type meshes often struggle to fully resolving these issues without a hyper-refined mesh or a priori knowledge about the solution. The MMPDE approach automatically concentrates mesh elements near the region where the solution exhibits large gradient, hence improves the computational efficiency. In this subsection, we give a brief overview of MMPDE. More details can be found in [33].

We consider an affine family of simplicial triangulations $\{\mathcal{T}_h\}$ for Ω . Denote by $(K, \mathcal{P}_1^K, \Sigma_K)$ the finite element space. Let N , N_v , and N_t denote the number of mesh elements, the number of vertices, and the number of time steps, respectively. Let $\mathbb{M} = \mathbb{M}(\mathbf{x})$ be a symmetric and uniformly positive definite metric tensor defined on Ω with $c_1\mathbb{I} \leq \mathbb{M}(\mathbf{x}) \leq c_2\mathbb{I}$ for all $\mathbf{x} \in \Omega$. We take the \mathbb{M} -uniform mesh approach that takes a nonuniform mesh and views it as a uniform one in the metric specified by \mathbb{M} . Essentially, \mathbb{M} controls the concentration and alignment of the mesh elements.

We consider two affine-equivalent finite elements, one for the reference elements and another for the physical mesh element. There exists an invertible affine mapping between the finite elements, denoted by F_K :

$$(\hat{K}, \mathcal{P}_1^{\hat{K}}, \Sigma_{\hat{K}}) \xrightarrow{F_K} (K, \mathcal{P}_1^K, \Sigma_K), \quad (13)$$

For each element $K \in \mathcal{T}_h$, denote by $F_K : \hat{K} \rightarrow K$ the affine mapping between K and the reference element \hat{K} so that $|\hat{K}| = 1$. Denote by \mathbf{x}_j^K for $j = 0, 1$, and 2 the vertices of K and $\boldsymbol{\xi}_j^{\hat{K}}$ the corresponding vertices of \hat{K} . Then the affine map F_K maps $\boldsymbol{\xi}_j^{\hat{K}}$ to \mathbf{x}_j^K , i.e. $F_K(\boldsymbol{\xi}_j^{\hat{K}}) = \mathbf{x}_j^K$ for $j = 0, 1$, and 2 . \hat{K} is called the reference element and belongs to $\hat{\mathcal{T}}_h$, the reference mesh.

Denote by \mathbb{M}_K the volume-average of \mathbb{M} over element K , i.e

$$\mathbb{M}_K = \frac{1}{|K|} \int_K \mathbb{M}(\mathbf{x}) d\mathbf{x},$$

and

$$\sigma_h = \sum_{K \in \mathcal{T}_h} \int_K \sqrt{\det(\mathbb{M}_K)} d\mathbf{x} = \sum_{K \in \mathcal{T}_h} |K| \sqrt{\det(\mathbb{M}_K)}.$$

F_K and \mathbb{M} give rise to the so-called equidistribution and alignment conditions in \mathbb{R}^2 :

1. equidistribution: $|K|\sqrt{\det(\mathbb{M}_K)} = \frac{\sigma_h}{N}$ for all $K \in \mathcal{T}_h$ and
2. alignment: $\frac{1}{2}\text{tr}(F'_K \mathbb{M}_K (F'_K)^T) = \sqrt{\det(F'_K \mathbb{M}_K (F'_K)^T)}$ for all $K \in \mathcal{T}_h$,

where F'_K is the Jacobian matrix of F_K . These two completely characterize a non-uniform mesh: the equidistribution condition controls the size and shape of mesh elements, while the alignment condition controls the orientation of mesh elements. The new physical mesh \mathcal{T}_h is found by minimizing the energy functional (also called the mesh functional) I given in discrete form by

$$I(\mathcal{T}_h) = \sum_{K \in \mathcal{T}_h} |K| G(\mathbb{J}_K, \det(\mathbb{J}_K), \mathbb{M}_K), \quad (14)$$

where $\mathbb{J}_K = (F'_K)^{-1}$ and

$$\begin{aligned} G(\mathbb{J}_K, \det(\mathbb{J}_K), \mathbb{M}_K) &= \alpha \sqrt{\det(\mathbb{M}_K)} (\text{tr}(\mathbb{J}_K \mathbb{M}_K \mathbb{J}_K^T))^p \\ &+ (1 - 2\alpha) 2^p \sqrt{\det(\mathbb{M}_K)} \left(\frac{\det(\mathbb{J}_K)}{\sqrt{\det(\mathbb{M}_K)}} \right)^p, \end{aligned} \quad (15)$$

with $\alpha \in (0, \frac{1}{2}]$ and $p > 1$ as dimensionless parameters. From numerical experiments, $\alpha = \frac{1}{3}$ and $p = \frac{3}{2}$ work well for most problems [34].

The moving mesh PDE (MMPDE) method is developed by Huang et al. [33] to find a new physical mesh by minimizing $I(\mathcal{T}_h)$, which is equivalent to the steepest descent method [35]. The MMPDE is a partial differential equation (also called the mesh PDE) that is given by

$$\frac{d\mathbf{x}_i}{dt} = -\frac{P_j}{\gamma} \left(\frac{\partial I}{\partial \mathbf{x}_i} \right)^T, \quad i = 1, \dots, N_v, \quad (16)$$

where γ is a user parameter meant to adjust the time scale of the mesh movement and $P_j = \det(\mathbb{M}(x_j))^{\frac{p-1}{2}}$ is chosen so that the MMPDE is invariant under the scaling transformation of \mathbb{M} . The physical PDE and mesh PDE can be solved either simultaneously or alternatively. When the PDEs are solved simultaneously, the mesh can respond quickly to any change in the physical solution. However, this procedure is highly nonlinear. In our work, we employ the alternative approach. The mesh PDE is firstly solved based on the physical solution and the mesh at the current time step. Then mesh nodes are relocated based on the solutions from mesh PDE. Lastly, the physical PDE is solved on the new mesh for the next time step. The alternate procedure allows for flexibility and potential efficiency at each time level. One disadvantage of this approach is a lag in time, which can be addressed by employing multiple iterations on the same time level before advancing to the next. It is always beneficial to start with a initially adapted mesh, especially when sharp layers exist from the beginning.

In this paper, for moving mesh for isotropic diffusion case, we use the metric tensor defined by

$$\mathbb{M} = \det(\mathbb{I} + |H_K(u)|)^{-\frac{1}{6}} (\mathbb{I} + |H_K(u)|), \quad (17)$$

where \mathbb{I} is the identity matrix, $H_K(u)$ is the recovered Hessian using least squares fitting to the values of the solution function at the mesh vertices, and $|H_K(u)| = \Lambda \text{diag}(|\lambda_1|, |\lambda_2|) \Lambda^T$ with $\Lambda \text{diag}(\lambda_1, \lambda_2) \Lambda^T$ being the eigen-decomposition of $H_K(u)$. The Hessian is computed $H(u)(\mathbf{x}_j) \approx H(q)(\mathbf{x}_j)$, where q is the algebraic polynomial determined by least squares fitting. For completeness, some details for the least squares fitting method (see Section 5.3 in [33]) are provided here.

Specifically, if u_j is the approximation of u at node $\mathbf{x}_j = (x_j, y_j)$ on mesh \mathcal{T}_h . Let \mathbf{x}_{j_i} for $i = 1, \dots, N_j$ be the N_j neighboring vertices near \mathbf{x}_j (including \mathbf{x}_j). Denote by \mathbf{x}_j^c the center of these points and define

$$H_j^x = \max_{i=1, \dots, N_j} |x_{j_i} - x_j^c|, \quad H_j^y = \max_{i=1, \dots, N_j} |y_{j_i} - y_j^c|. \quad (18)$$

Then the polynomial q in (Legendre) polynomial form

$$q(x, y) = \sum_{k=0}^2 \sum_{m=0}^{2-k} a_{k,m} P_k \left(\frac{x - x_j^c}{H_j^x} \right) P_m \left(\frac{y - y_j^c}{H_j^y} \right), \quad (19)$$

and is determined by

$$\min_{a_{0,0}, \dots, a_{2,0}} \sum_{i=1}^{N_j} (q(x_{j_i}, y_{j_i}) - u_{j_i})^2. \quad (20)$$

Then $\nabla u(\mathbf{x}_j) \approx \nabla q(\mathbf{x}_j)$. This metric tensor is optimal in the L^2 norm of linear interpolation error on triangular meshes [35]. Moreover, it is clearly symmetric and one may replace $|H_K(u)|$ with $\alpha^{-1}|H_K(u)|$, where α is called the intensity parameter and helps ensure that \mathbb{M} is positive definite. This monitor function is derived on anisotropic error estimates (see [33], chapter 5, for a more detailed discussion and the derivation of (17) and choice of α).

2.3 Moving mesh with Streamline Upwind Petrov-Galerkin (MM-SUPG) method

Now we apply the MMPDE method to solve the SUPG formulation (6). Write $\mathbf{u}_h(\mathbf{x}, t) = \sum_{j=1}^N u_j(t) \varphi_j(\mathbf{x})$, where $\{\varphi_j\}_{j=1}^N$ is the set of linear basis functions in U_h^0 . Also, since φ_j is a linear function, the element-wise integral average can be defined explicitly

$$\frac{1}{|K|} \int_K \varphi_j \varphi_i d\mathbf{x} = \begin{cases} \frac{1}{(d+1)(d+2)} & \text{for } i \neq j \\ \frac{2}{(d+1)(d+2)} & \text{for } i = j \end{cases}. \quad (21)$$

Approximate the global integral as

$$\int_{\Omega} g(\mathbf{x}, t) d\mathbf{x} = \sum_{K \in \mathcal{T}_h} |K| \int_K g(\mathbf{x}, t) d\mathbf{x} \quad (22)$$

$$\approx \sum_{K \in \mathcal{T}_h} |K| \sum_{j=1}^m \lambda_j g(\boldsymbol{\omega}_j), \quad (23)$$

where $\boldsymbol{\omega}_j$ are the quadrature nodes for element K and λ_j are weights such that $\sum_{j=1}^m \lambda_j = 1$. For any tensor \mathbb{F} , we then define the element-wise average by

$$\mathbb{F}_K = \frac{1}{|K|} \int_K \mathbb{F}(\mathbf{x}) d\mathbf{x} \approx \sum_{j=1}^N \lambda_j \mathbb{F}(\boldsymbol{\omega}_j). \quad (24)$$

The semi-discrete matrix formulation for (6) is given by

$$\mathbf{M}\mathbf{u}'_h(t) + \mathbf{A}(t)\mathbf{u}_h(t) = \mathbf{f}(t), \quad (25)$$

where $\mathbf{u} = [u_1, \dots, u_{Nv}]^T$, \mathbf{M} , \mathbf{A} , and \mathbf{b} are given by

$$M_{ij} = \sum_{K \in \mathcal{T}_h} (\varphi_j, \varphi_i)_{0,K} + \tau_K (\varphi_j, \mathbf{b} \cdot \nabla \varphi_i)_{0,K} \quad (26)$$

$$A_{ij}(t) = \sum_{K \in \mathcal{T}_h} (\mathbf{b} \cdot \nabla \varphi_j, \varphi_i)_{0,K} + |K| (\nabla \varphi_i)^T \varepsilon \mathbb{D}_K \nabla \varphi_j \\ + \tau_K ((\mathbf{b} \cdot \nabla \varphi_j, \mathbf{b} \cdot \nabla \varphi_i)_{0,K} + (\varepsilon \mathbb{D}_K \nabla \varphi_j, \nabla (\mathbf{b} \cdot \nabla \varphi_i))_{0,K}) \quad (27)$$

$$f_i(t) = \sum_{K \in \mathcal{T}_h} (f, \varphi_i)_{0,K} + \tau_K (f, \mathbf{b} \cdot \nabla \varphi_i)_{0,K}. \quad (28)$$

Denote N_t as the number of time steps. We use a θ scheme to discretize in time. For (25), we approximate

$$\mathbf{u}'_h(t) \approx \frac{\mathbf{u}_h(t_{m+1}) - \mathbf{u}_h(t_m)}{\Delta t}, \quad m = 1, \dots, N_t. \quad (29)$$

Then the corresponding θ -scheme is given by

$$M \frac{\mathbf{u}_h(t_{m+1}) - \mathbf{u}_h(t_m)}{\Delta t} + \theta \mathbf{A} \mathbf{u}_h(t_{m+1}) + (1 - \theta) \mathbf{A} \mathbf{u}_h(t_m) \\ = \theta \mathbf{f}(t_{m+1}) + (1 - \theta) \mathbf{f}(t_m), \quad m = 1, \dots, N_t. \quad (30)$$

Grouping the $\mathbf{u}_h(t_{m+1})$ terms, we may rewrite (30) as

$$\left(\frac{M}{\Delta t} + \theta \mathbf{A} \right) \mathbf{u}_h(t_{m+1}) = \theta \mathbf{f}(t_{m+1}) + (1 - \theta) \mathbf{f}(t_m) + \left(\frac{M}{\Delta t} - (1 - \theta) \mathbf{A} \right) \mathbf{u}_h(t_m), \quad (31)$$

for $m = 1, \dots, N_t$. Hence, we may write a system of ODEs

$$\tilde{\mathbf{A}} \mathbf{u}_h(t_{m+1}) = \tilde{\mathbf{f}}^{m+1}, \quad m = 1, \dots, N_t, \quad (32)$$

where

$$\tilde{\mathbf{A}} = \mathbf{M} + \theta \Delta t \mathbf{A} \quad (33)$$

$$\tilde{\mathbf{f}}^{m+1} = \theta \Delta t \mathbf{f}(t_{m+1}) + \Delta t (1 - \theta) \mathbf{f}(t_m) + (\mathbf{M} - \Delta t (1 - \theta) \mathbf{A}) \mathbf{u}_h(t_m). \quad (34)$$

In this work, we use $\theta = 0.5$, which corresponds to the Crank-Nicholson. Fixed time step is used in the computations. In Section 2 we establish bounds on Δt so that DMP is satisfied.

3 Results for Isotropic Diffusion

Now, we present some numerical examples for isotropic diffusion case where we take the diffusivity tensor \mathbb{D} as an identity matrix. The value of diffusivity is given by ε . We consider two different examples and compare results from four different methods: fixed mesh finite element method (FM-FEM) without SUPG, fixed mesh finite element method with SUPG (FM-SUPG), moving mesh finite element method (MM-FEM) without SUPG (which is the MMPDE method), and our moving mesh with SUPG (MM-SUPG) method. We denote the MMPDE method as MM-FEM for consistency in what follows.

Example 3.1. This example is similar to the simulated example presented in [36]. The domain is $\Omega = (0, 10) \times (-1.25, 1.25)$ and an initial smooth solution is given by

$$u_0(x, y) = e^{-\frac{(x-1)^2+y^2}{0.25}} + e^{-\frac{(x-1)^2+(y-0.5)^2}{0.25}} + e^{-\frac{(x-1)^2+(y+0.5)^2}{0.25}}, \quad (35)$$

The velocity field is given by

$$\mathbf{b} = \left(1 - \exp(\theta x) \cos(2\pi y), \frac{\theta}{2\pi} \exp(\theta x) \sin(2\pi y) \right), \quad (36)$$

with

$$\theta = \frac{1}{2\varepsilon} - \sqrt{\left(\frac{1}{2\varepsilon}\right)^2 + 4\pi^2}. \quad (37)$$

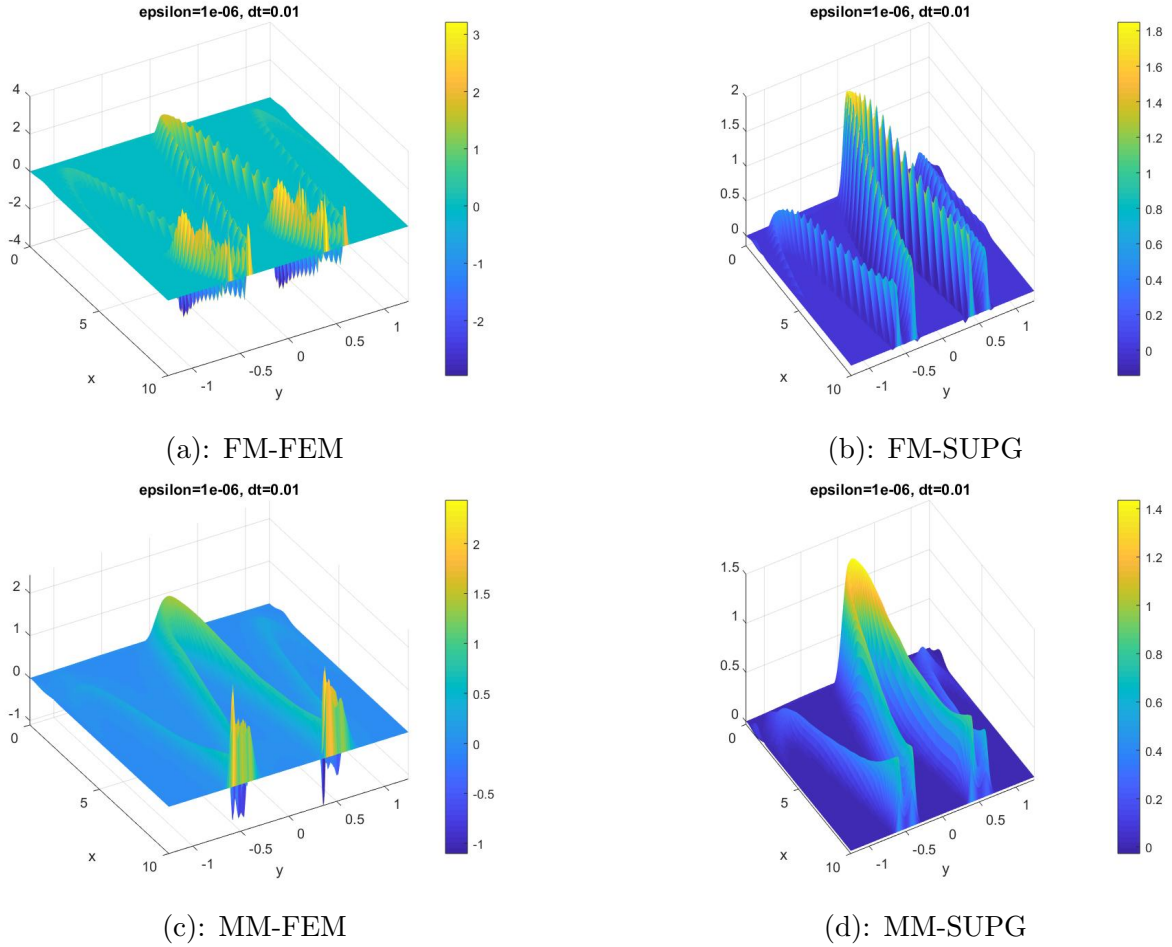


Figure 1: Example 3.1 – side view of four different methods with $\Delta t = 0.01$, \mathbf{b} is given by (36), $N = 32,768$ at $T = 5.0$.

For this example, $\varepsilon = 10^{-6}$ is used in the computation, which gives $\theta \approx -3.948 \times 10^{-5}$. We compute the diffusion of the initial solution from 0 to 5 seconds with Dirichlet boundary conditions. Time step

$\Delta t = 10^{-2}$ and $N = 32,768$ elements are used in the computations. Allowing the convection process to be carried out, we see fine layers form on the interior and boundary of Ω .

The results are shown in Figure 1 with side view profiles and Figure 2 with top view profiles. From Figures 1(a) and (c), we see that for the classic Galerkin method, both FM-FEM and MM-FEM, the numerical solutions have non-physical oscillations form near the outflow boundary at $x = 10$. Figure 1(b) shows that FM-SUPG resolves the boundary layers present in FM-FEM and MM-FEM but has artificial oscillations on the interior of Ω . On the other hand, Figure 1(d) shows that MM-SUPG results in the smoothest surface among all four methods, and both interior oscillations and oscillations near the outflow have been resolved. Even with smaller Δt as 5×10^{-3} , we see in Figure 2 that MM-FEM still has layers at the outflow, where MM-SUPG performs much better.

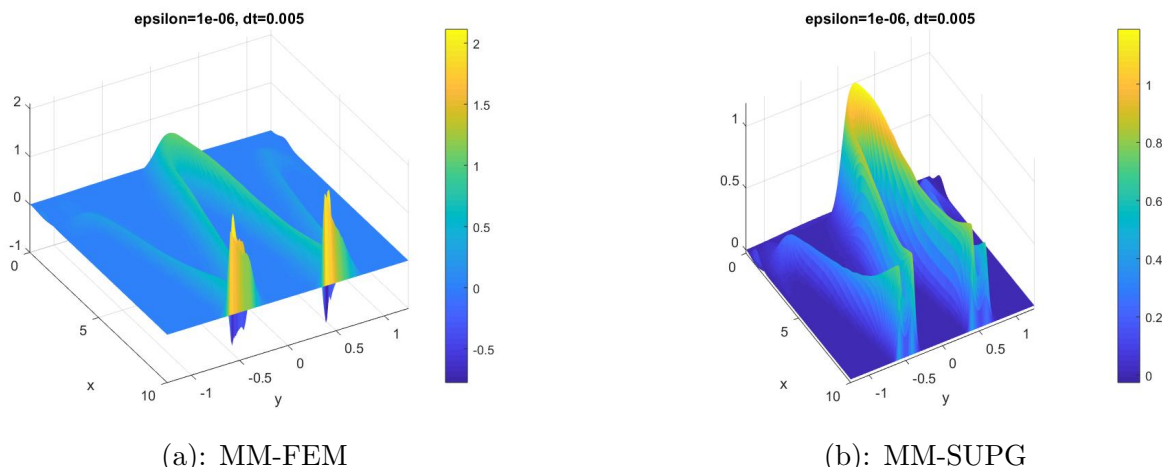


Figure 2: Example 3.1 – side view of MM-FEM and MM-SUPG methods with $\Delta t = 0.005$, \mathbf{b} is given by (36), $N = 32,768$ at $T = 5.0$.

Example 3.2. Here we consider another example (taken from [16]) with exact solution

$$u(x, y, t) = 16 \sin(\pi t) x(1-x)y(1-y) \times \left(\frac{1}{2} + \frac{1}{\pi} \arctan \left(2\varepsilon^{-1/2} (0.25^2 - (x-0.5)^2 - (y-0.5)^2) \right) \right), \quad (38)$$

with Dirichlet boundary conditions. We compute to time $T = 0.5$ with time step $\Delta t = 10^{-3}$. The severity of the interior layer is proportional to ε and its thickness is $\sqrt{\varepsilon}$. We also use $\mathbf{b} = (2, 3)$ and $\varepsilon = 10^{-6}$.

For coarse mesh with fewer elements (that is, smaller N), we observe artificial oscillations in the direction of \mathbf{b} , including MM-FEM, for example, with $N = 8192$. Increasing the number of mesh elements helps to improve the results for MM-FEM. Figure 3 shows the top view of the solutions at $T = 0.5$ for the four different methods with $N = 32768$, while Figure 4 displays the side view of the solution profiles. As can be seen, significant smearing occurs in the solution obtained using the FM-FEM and FM-SUPG, though the latter shows an improvement. On the other hand, both the MM-FEM and MM-SUPG perform well with $N = 32768$ elements in the mesh. This is supported by the H^1 -seminorm errors in Table 1 and cap view in Figure 5. The L^2 -norm errors in Table 2 shows that MM-SUPG performs a bit better than MM-FEM for this example. We observe pronounced mesh movement in the direction of \mathbf{b} for MM-FEM and MM-SUPG, as shown in Figure 6. The rate of convergence in the H^1 -seminorm and L^2 norm are shown in Figure 7.

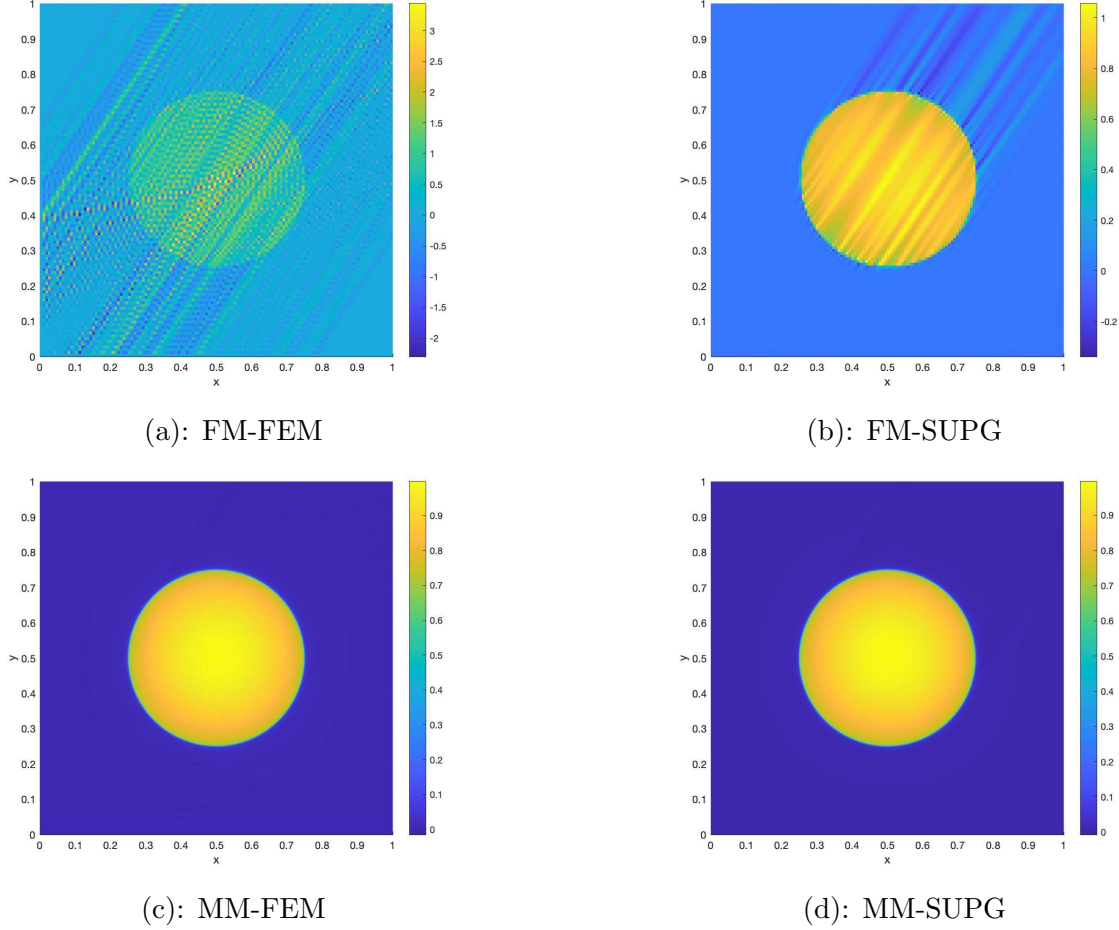


Figure 3: Example 3.2 – top view with four different methods with $\Delta t = 0.001$ for $\mathbf{b} = (2, 3)$, $N = 32768$ at $T = 0.5$.

Table 1: Example 3.2 – H^1 -seminorm errors for $\varepsilon = 10^{-6}$ at $\Delta t = 0.001$ for $\mathbf{b} = (2, 3)$.

N	MM-FEM	MM-SUPG	FM-FEM	FM-SUPG
512	12.1038	10.9715	27.6628	18.3147
2048	10.5624	11.0912	26.7879	15.3485
8192	4.4580	4.3027	34.9201	14.7499
32768	0.7387	0.9278	39.3491	10.7836
131072	0.2657	0.2101	39.2190	7.7920

Within this example, we also consider a time-dependent flow given by $\mathbf{b} = (y - t, x - t)$. The convergence rates in the H^1 -seminorm and L^2 norm can be found in Figure 8, where numerical values are recorded in Tables 3 and 4. Again, both MM-FEM and MM-SUPG perform much better than FM-FEM and FM-SUPG with larger N .

We see small oscillations along the top of the surface in the direction of the outflow in Figures 5 and 9, even for large N . However, for larger N , we see that DMP is not violated. Both methods converge to the same approximate solution as N increases. In Figure 4 we see that the MM-SUPG

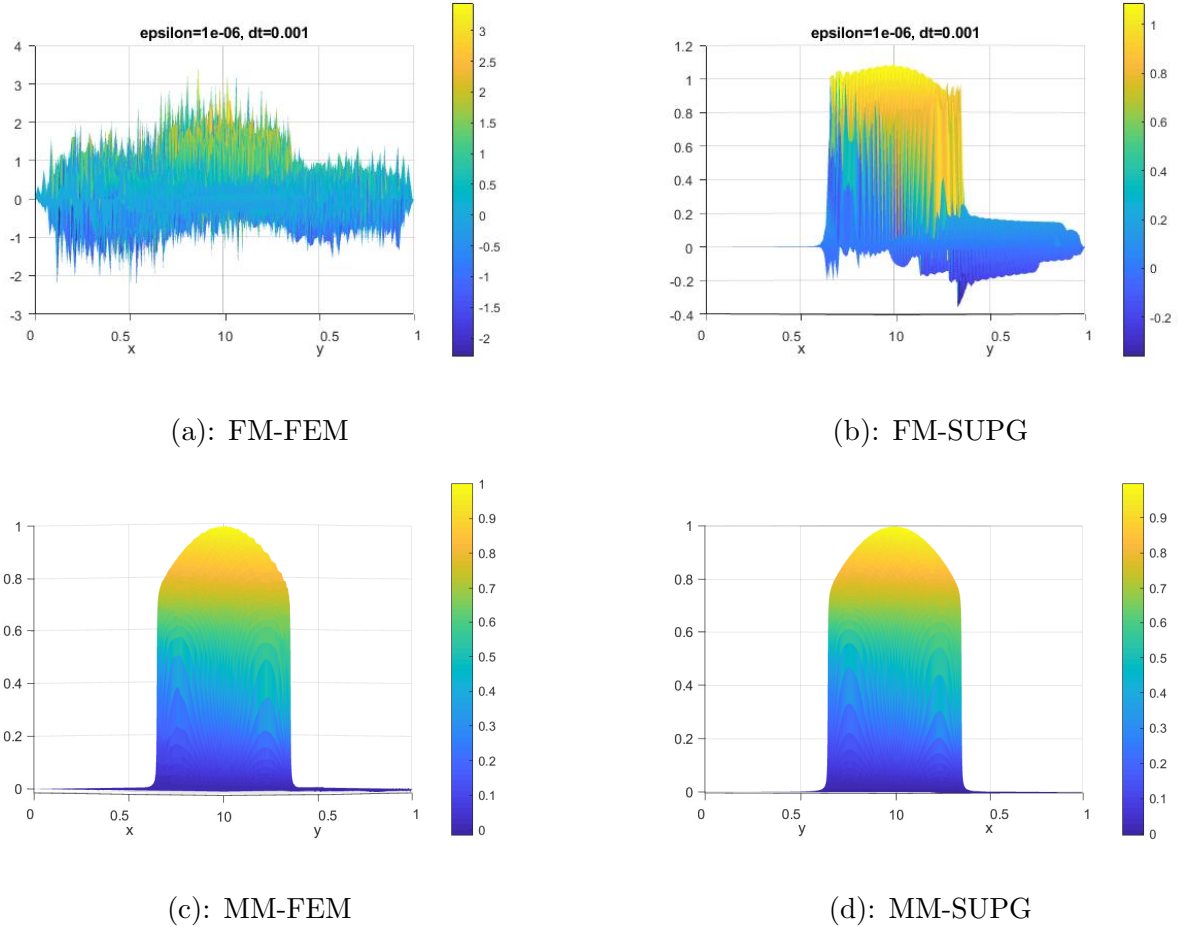
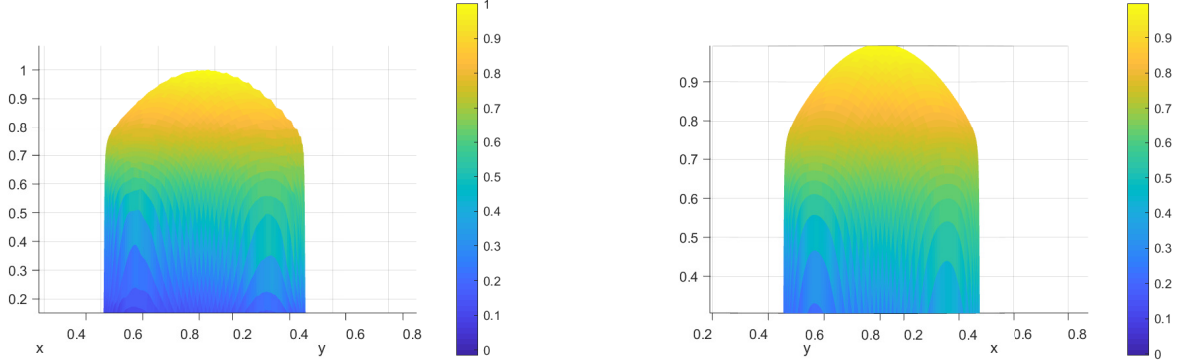


Figure 4: Example 3.2 – side view with the four different methods with $\Delta t = 0.001$, $\mathbf{b} = (2, 3)$, $N = 32768$ at $T = 0.5$.

Table 2: Example 3.2 – L^2 norm errors for $\varepsilon = 10^{-6}$ at $\Delta t = 0.001$ for $\mathbf{b} = (2, 3)$.

N	MM-FEM	MM-SUPG	FM-FEM	FM-SUPG
512	0.2633	0.1289	1.5475	0.4138
2048	0.1127	0.0823	0.8708	0.2871
8192	0.0475	0.0096	0.5818	0.1573
32768	0.0019	0.0010	0.3720	0.0510
131072	0.0004	0.0003	0.1995	0.0180

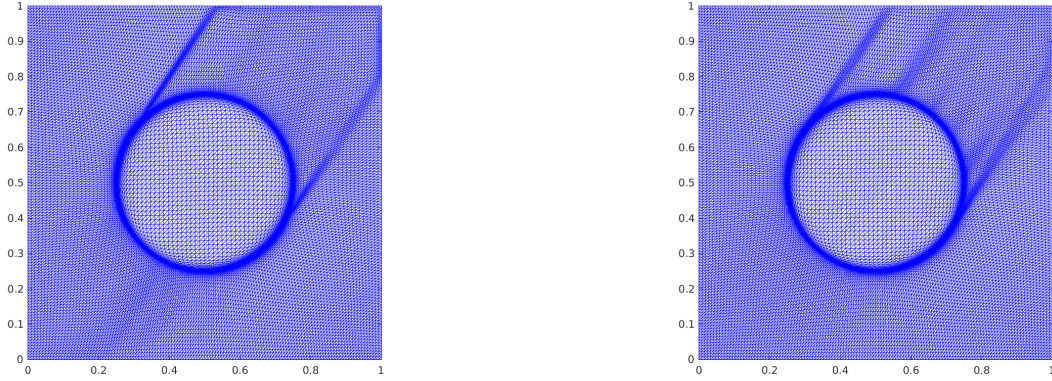
method is a noticeable improvement compared to all methods. In Figure 9, only slight oscillations are observable on the backside of the surface (in the direction of the streamlines) for MM-FEM. This is more prominent for smaller N in the MM-FEM case. Overall, MM-SUPG performs the best among all the four methods under consideration.



(a): MM-FEM

(b): MM-SUPG

Figure 5: Example 3.2 – cap view moving mesh with $\Delta t = 0.001$, $\mathbf{b} = (2, 3)$, $N = 32768$ at $T = 0.5$.



(a): MM-FEM

(b): MM-SUPG

Figure 6: Example 3.2 – Mesh movement for $T = 0.5$ and $\mathbf{b} = (2, 3)$, $N = 32768$ at $T = 0.5$.

4 Discrete Maximum Principle for Anisotropic Diffusion

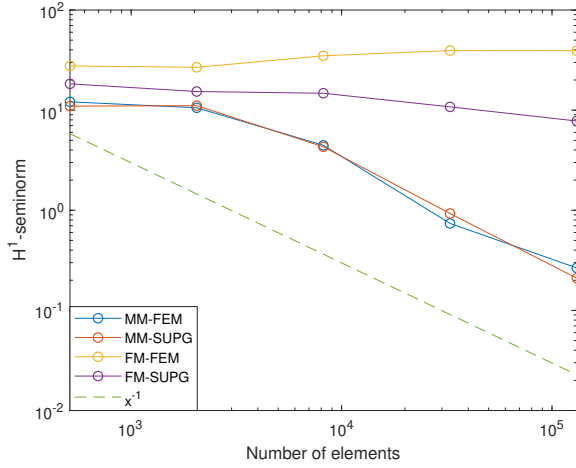
In this section, we consider the anisotropic diffusion case where the diffusivity tensor \mathbb{D} has different eigenvalues, which indicates diffusion is faster in one direction (the principal diffusion direction) than in the other direction.

We say the solution u to (1) satisfies the weak maximum principle if $u \in C^{2,1}(\Omega_T) \cap C(\bar{\Omega}_T)$ and $f \leq 0$ in Ω_T [37]:

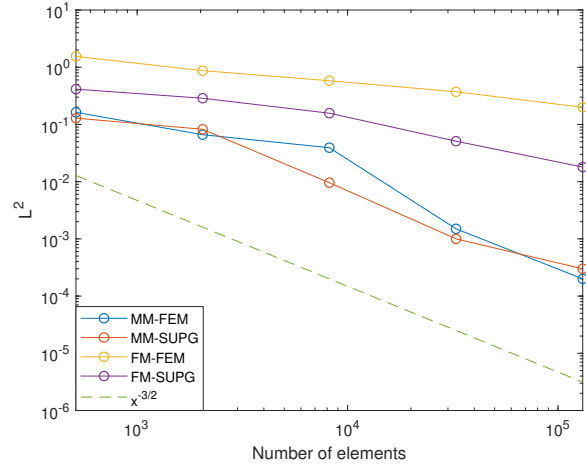
$$\max_{(\mathbf{x}, t) \in \bar{\Omega}_T} u \leq \max \left\{ 0, \max_{(\mathbf{x}, t) \in \Gamma_T} u(\mathbf{x}, t) \right\}, \quad (39)$$

where $\Gamma_T = \bar{\Omega}_T - \Omega_T$ is the parabolic boundary.

Let S_i^K be the face opposite to the vertex \mathbf{a}_i^K , the i th vertex of element K . Introduce \mathbf{q} vectors as



(a): H^1 -seminorm error.



(b): L^2 norm error.

Figure 7: Example 3.2 – H^1 -seminorm and L^2 norm errors with $\varepsilon = 10^{-6}$ and $\Delta t = 0.001$ with flow field $\mathbf{b} = (2, 3)$ at $T = 0.5$.

Table 3: Example 3.2 – H^1 -seminorm errors for $\varepsilon = 10^{-6}$ at $\Delta t = 0.001$ for $\mathbf{b} = (y - t, x - t)$.

N	MM-FEM	MM-SUPG	FM-FEM	FM-SUPG
512	11.1473	11.7017	16.7382	16.6045
2048	10.6529	9.7031	13.0265	12.8651
8192	5.8337	4.7036	12.9658	12.3947
32768	0.7614	0.9654	11.0075	9.8446
131072	0.1614	0.2054	8.7996	7.1405

[26]:

$$\mathbf{q}_i^K = \frac{\mathbf{n}_i^K}{h_i^K}, \quad (40)$$

where \mathbf{n}_i^K is the unit inward normal pointing to \mathbf{a}_i^K , and h_i^K is the distance from vertex \mathbf{a}_i to surface S_i . Figure 10 shows an illustration of \mathbf{q} vectors.

In [38] it was shown that

$$\nabla \varphi_i|_K = \mathbf{q}_i^K. \quad (41)$$

Table 4: Example 3.2 – L^2 errors for $\varepsilon = 10^{-6}$ at $\Delta t = 0.001$ for $\mathbf{b} = (y - t, x - t)$.

N	MM-FEM	MM-SUPG	FM-FEM	FM-SUPG
512	0.1629	0.1181	0.3340	0.1843
2048	0.0662	0.0530	0.2326	0.1193
8192	0.0392	0.0130	0.1724	0.0903
32768	0.0015	0.0011	0.1175	0.0411
131072	0.0002	0.0002	0.0602	0.0161

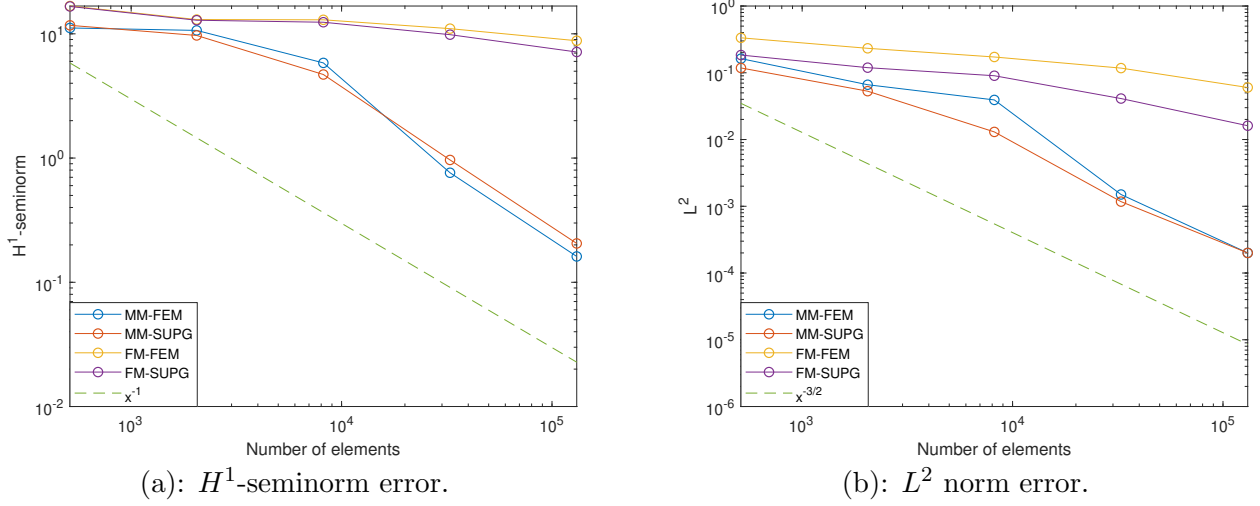


Figure 8: Example 3.2 – H^1 -seminorm and L^2 norm errors with $\varepsilon = 10^{-6}$ and $\Delta t = 0.001$ with flow field $\mathbf{b} = (y - t, x - t)$ at $T = 0.5$.

Therefore,

$$\int_K (\nabla \varphi_i)^2 d\mathbf{x} = \|\mathbf{q}\|^2 |K| = \frac{|K|}{(h_i^K)^2}. \quad (42)$$

We also have the following inequality due to the Divergence Theorem:

$$\int_K \varphi_i (\mathbf{b} \cdot \nabla \varphi_i) d\mathbf{x} = -\frac{1}{2} \int_K (\nabla \cdot \mathbf{b}) \varphi_i^2 d\mathbf{x}. \quad (43)$$

Following [26], we define the diffusion-dependent map $\mathbb{D}_K^{-1/2} \mathbf{x} : K \rightarrow \tilde{K}$. Define the \mathbb{D}_K -norm by $\|\mathbf{x}\|_{\mathbb{D}_K} = \sqrt{\mathbf{x}^T \mathbb{D}_K \mathbf{x}}$. Then we have the following relations

$$\tilde{\mathbf{a}}_i^K = \mathbb{D}_K^{-1/2} \mathbf{a}_i^K, \quad \tilde{S}_i^K = \mathbb{D}_K^{-1/2} S_i^K, \quad |\tilde{K}| = \det(\mathbb{D}_K)^{1/2} |K|, \quad \tilde{\mathbf{q}}_i^K = \mathbb{D}_K^{1/2} \mathbf{q}_i^K, \quad \tilde{h}_i^K = \|\tilde{\mathbf{q}}_i^K\|^{-1}. \quad (44)$$

Denote by $\tilde{\alpha}_{ij}^K$ the dihedral angle between surfaces \tilde{S}_i^K and \tilde{S}_j^K . Then

$$\cos(\tilde{\alpha}_{ij}^K) = -\frac{(\tilde{\mathbf{q}}_i^K)^T \tilde{\mathbf{q}}_j^K}{\|\tilde{\mathbf{q}}_i^K\| \|\tilde{\mathbf{q}}_j^K\|} = -\frac{(\mathbf{q}_i^K)^T \mathbb{D}_K \mathbf{q}_j^K}{\|\mathbf{q}_i^K\|_{\mathbb{D}_K} \|\mathbf{q}_j^K\|_{\mathbb{D}_K}}, \quad i \neq j. \quad (45)$$

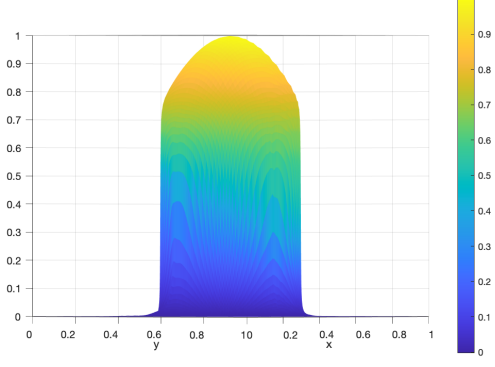
Similarly, on the element K , we have the relation

$$\cos(\alpha_{ij}) = -\mathbf{n}_i \cdot \mathbf{n}_j = -\frac{\mathbf{q}_i \cdot \mathbf{q}_j}{\|\mathbf{q}_i\| \|\mathbf{q}_j\|}. \quad (46)$$

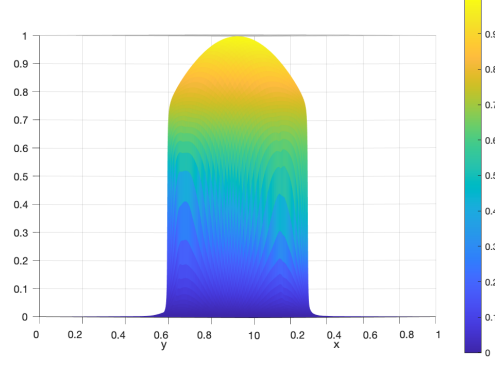
It follows from (40) that

$$\frac{h_i^K}{\sqrt{\rho_{\max}(\mathbb{D}_K)}} \leq \tilde{h}_i^K \leq \frac{h_i^K}{\sqrt{\rho_{\min}(\mathbb{D}_K)}}, \quad (47)$$

where $\rho_{\min}(\mathbb{D}_K)$ and $\rho_{\max}(\mathbb{D}_K)$ are the min and max eigenvalues of \mathbb{D}_K , respectively.



(a): MM-FEM



(b): MM-SUPG



(c): Enlarged view of (a)



(d): Enlarged view of (b)

Figure 9: Example 3.2 – side view with $\Delta t = 0.001$ and $\mathbf{b} = (y - t, x - t)$, $\varepsilon = 10^{-6}$, and $N = 32768$ for MM-FEM and MM-SUPG at $T = 0.5$.

The difficulty with the finite element formulation mentioned in Section 2 is the coupling of the diffusion tensor with the flow field \mathbf{b} in (27) as follows:

$$(\mathbb{D}\nabla u_h, \nabla(\mathbf{b} \cdot \nabla \varphi^h))_{0,K}. \quad (48)$$

For general $\mathbf{b} = (b_1(x_1, x_2), b_2(x_1, x_2))$, consider

$$\frac{\partial \mathbf{b}}{\partial x_i} \otimes \mathbb{D}_{(i)}, \quad i = 1, \dots, d, \quad (49)$$

where \mathbb{D}_i is the vector i th row of \mathbb{D} . An essential ingredient to the following analysis is that the tensor defined by

$$\mathbb{K} = \sum_{i=1}^d \frac{\partial \mathbf{b}}{\partial x_i} \otimes \mathbb{D}_{(i)} \quad (50)$$

is symmetric and positive definite. This highlights a significant relationship between $\frac{\partial \mathbf{b}}{\partial x_i}$ and the i th row of \mathbb{D} when using SUPG. The added diffusion integral term in (6) can be written in general form

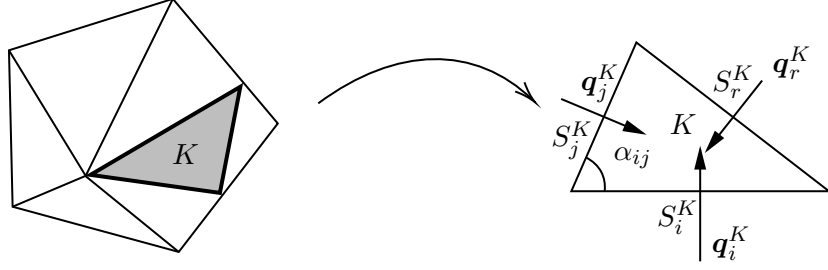


Figure 10: Illustration of faces and \mathbf{q} vectors.

as

$$\tau_K \int_K (\mathbb{D} \nabla u) \cdot \nabla (\mathbf{b} \cdot \nabla v) d\mathbf{x} = \tau_K \sum_{i=1}^d \int_K (\nabla v)^T \left(\frac{\partial \mathbf{b}}{\partial x_i} \otimes \mathbb{D}_{(i)} \right) \nabla u d\mathbf{x} \quad (51)$$

One may view \mathbb{K} as a kind of weighted diffusion tensor.

The analysis of the numerical scheme relies on the following fundamental lemma [39].

Lemma 4.1. *If $\tilde{\mathbf{A}}$ in (32) is an M -matrix and has nonnegative row sums, then the numerical scheme satisfies DMP.*

The following lemmas were used in [25] to analyze DMP with $\mathbf{b} = \mathbf{0}$.

Lemma 4.2. *If the mesh satisfies the anisotropic nonobtuse angle condition (ANAC)*

$$0 < \tilde{\alpha}_{ij}^K \leq \frac{\pi}{2}, \quad \forall i, j = 1, \dots, d+1, i \neq j, \forall K \in \mathcal{T}_h, \quad (52)$$

then for any \mathbb{F}_K of SPD-type, the matrix defined by

$$\sum_{K \in \mathcal{T}_h} |K| (\nabla \varphi_i)^T \mathbb{F}_K \nabla \varphi_j, \quad i = 1, \dots, N_v, j = 1, \dots, N_v \quad (53)$$

is an M -matrix and has nonnegative row sums. Moreover, for any element $K \in \mathcal{T}_h$, and $i, j = 1, \dots, d+1$,

$$(\nabla \varphi_i)^T \mathbb{F}_K \nabla \varphi_j = \begin{cases} -\frac{\cos(\tilde{\alpha}_{ij}^K)}{\tilde{h}_i^K \tilde{h}_j^K} & \text{for } i \neq j \\ \frac{1}{(\tilde{h}_i^K)^2} & \text{for } i = j. \end{cases} \quad (54)$$

When $d = 2$, the case $i \neq j$ simplifies to

$$|K| (\nabla \varphi_i)^T \mathbb{F}_K \nabla \varphi_j = -\frac{\sqrt{\det(\mathbb{F}_K)}}{2} \cot(\tilde{\alpha}_{ij}^K). \quad (55)$$

We establish DMP in a series of steps. We first investigate spatial estimates, which are critical to understanding the required structure of the matrices \mathbf{A} and \mathbf{M} . Temporal estimates are then derived in order to apply Lemma 4.1.

4.1 General flow forms

In this section we investigate the structure of \mathbb{K} specified by \mathbf{b} . For $d = 2$, we have

$$\frac{\partial \mathbf{b}}{\partial x_1} \otimes \mathbb{D}_{(1)} = \begin{pmatrix} \frac{\partial b_1}{\partial x_1} D_{11} & \frac{\partial b_1}{\partial x_1} D_{12} \\ \frac{\partial b_2}{\partial x_1} D_{11} & \frac{\partial b_2}{\partial x_1} D_{12} \end{pmatrix} \quad (56)$$

and

$$\frac{\partial \mathbf{b}}{\partial x_2} \otimes \mathbb{D}_{(2)} = \begin{pmatrix} \frac{\partial b_1}{\partial x_2} D_{21} & \frac{\partial b_1}{\partial x_2} D_{22} \\ \frac{\partial b_2}{\partial x_2} D_{21} & \frac{\partial b_2}{\partial x_2} D_{22} \end{pmatrix}. \quad (57)$$

There are two ways in which we consider \mathbb{K} . If (56) and (57) are of SPD-type, then \mathbb{K} will be as well. If not, then we need to analyze \mathbb{K} in its general form given by

$$\mathbb{K} = \begin{pmatrix} \frac{\partial b_1}{\partial x_1} D_{11} + \frac{\partial b_1}{\partial x_2} D_{21} & \frac{\partial b_1}{\partial x_1} D_{12} + \frac{\partial b_1}{\partial x_2} D_{22} \\ \frac{\partial b_2}{\partial x_1} D_{11} + \frac{\partial b_2}{\partial x_2} D_{21} & \frac{\partial b_2}{\partial x_1} D_{12} + \frac{\partial b_2}{\partial x_2} D_{22} \end{pmatrix}. \quad (58)$$

Hence, using the symmetric condition, we would require

$$\frac{\partial}{\partial x_1} (b_2 D_{11} - b_1 D_{12}) = \frac{\partial}{\partial x_2} (b_1 D_{22} - b_2 D_{21}). \quad (59)$$

Assume first that these matrices are of SPD-type so that general form of \mathbb{K} is of SPD-type.

Theorem 4.3. *Suppose \mathbb{D} , equations (56), and (57) are of SPD-type with constant real-valued entries and $D_{12} = D_{21} \neq 0$. Then there are functions $f_1(x_2, t)$, $g_1(x_2, t)$, $f_2(x_1, t)$, and $g_2(x_1, t)$ such that*

$$b_1(x_1, x_2, t) = \frac{D_{11} D_{22} f_1(x_1, t) - D_{12} D_{21} f_2(x_2, t)}{\det(\mathbb{D})} \quad (60)$$

and

$$b_2(x_1, x_2, t) = \frac{D_{12} D_{22} (f_1(x_1, t) - f_2(x_2, t))}{\det(\mathbb{D})}. \quad (61)$$

for $D_{22} \neq 0$. Likewise,

$$b_1(x_1, x_2, t) = \frac{D_{11} D_{21} (g_2(x_2, t) - g_1(x_1, t))}{\det(\mathbb{D})} \quad (62)$$

and

$$b_2(x_1, x_2, t) = \frac{D_{11} D_{22} g_2(x_2, t) - D_{12} D_{21} g_1(x_1, t)}{\det(\mathbb{D})}, \quad (63)$$

whenever $D_{11} \neq 0$.

Proof. Assume $D_{12} = D_{21} \neq 0$ and $D_{22} \neq 0$. The other case is very similar. Assuming symmetry as mentioned, we have

$$\frac{\partial b_1}{\partial x_1} = \left(\frac{D_{11}}{D_{12}} \right) \frac{\partial b_2}{\partial x_1} \quad (64)$$

$$b_1(x_1, x_2, t) = \left(\frac{D_{11}}{D_{12}} \right) b_2(x_1, x_2, t) + f_2(x_2, t), \quad (65)$$

for some $f_2(x_2, t)$. Additionally,

$$\frac{\partial b_1}{\partial x_2} = \left(\frac{D_{21}}{D_{22}} \right) \frac{\partial b_2}{\partial x_2} \quad (66)$$

$$b_1(x_1, x_2, t) = \left(\frac{D_{21}}{D_{22}} \right) b_2(x_1, x_2, t) + f_1(x_1, t), \quad (67)$$

for some function $f_1(x_1, t)$. Equating the two equations for b_1 gives

$$\left(\frac{D_{11}}{D_{12}} \right) b_2(x_1, x_2, t) + f_2(x_2, t) = \left(\frac{D_{21}}{D_{22}} \right) b_2(x_1, x_2, t) + f_1(x_1, t) \quad (68)$$

$$\left(\frac{D_{11}}{D_{12}} - \frac{D_{21}}{D_{22}} \right) b_2(x_1, x_2, t) = f_1(x_1, t) - f_2(x_2, t) \quad (69)$$

$$b_2(x_1, x_2, t) = \frac{D_{12}D_{22}(f_1(x_1, t) - f_2(x_2, t))}{\det(\mathbb{D})}. \quad (70)$$

Plugging this into the equation for b_1 , we have

$$b_1(x_1, x_2, t) = \left(\frac{D_{11}}{D_{12}} \right) \frac{D_{12}D_{22}(f_1(x_1, t) - f_2(x_2, t))}{\det(\mathbb{D})} + f_2(x_2, t) \quad (71)$$

$$= \frac{D_{11}D_{22}(f_1(x_1, t) - f_2(x_2, t)) + f_2(x_2, t)(D_{11}D_{22} - D_{12}D_{21})}{\det(\mathbb{D})} \quad (72)$$

$$= \frac{D_{11}D_{22}f_1(x_1, t) - D_{12}D_{21}f_2(x_2, t)}{\det(\mathbb{D})}. \quad (73)$$

Note that since \mathbb{D} is of SPD-type, $\det(\mathbb{D}) \neq 0$. □

Remark 4.1. If $D_{12} = D_{21}$ is not zero, the general form of \mathbf{b} is given by

$$\frac{1}{\det(\mathbb{D})} (D_{22}f_1(x_1, t)\mathbb{D}_{(1)} - D_{12}f_2(x_2, t)\mathbb{D}_{(2)}) \quad (74)$$

for some functions f_1 and f_2 whenever $D_{22} \neq 0$. Similarly, if $D_{11} \neq 0$, then the general form of \mathbf{b} is given by

$$\frac{1}{\det(\mathbb{D})} (D_{11}g_2(x_2, t)\mathbb{D}_{(2)} - D_{21}g_1(x_1, t)\mathbb{D}_{(1)}) \quad (75)$$

If D_{11} and D_{22} are both not zero, then $g_1 = -\frac{D_{22}}{D_{21}}f_1$ and $g_2 = -\frac{D_{12}}{D_{11}}f_2$.

Corollary 4.3.1. *If $\mathbb{D} = \text{diag}(D_{11}, D_{22})$, with D_{11} and $D_{22} \neq 0$, then there are functions f and g such that*

$$\mathbf{b}(x_1, x_2, t) = \begin{pmatrix} f(x_1, t) \\ \frac{D_{11}}{D_{22}} g(x_2, t) \end{pmatrix} \quad (76)$$

and

$$\mathbb{K} = \begin{pmatrix} \frac{\partial f}{\partial x_1} & 0 \\ 0 & \frac{\partial g}{\partial x_2} \end{pmatrix}. \quad (77)$$

Proof. The form of \mathbf{b} as shown in (76) follows from a similar argument as shown in the proof of the previous theorem. \square

Based on the Remark 4.1, we require

$$\frac{D_{22}}{\det(\mathbb{D})} \left(D_{11} \frac{\partial f_1}{\partial x_1} - D_{12} \frac{\partial f_2}{\partial x_2} \right). \quad (78)$$

to share the same sign as the divergence of \mathbf{b} .

4.2 Mass and stiffness matrix structure: estimates on τ_K

We first establish non-negative diagonal entries for the mass and stiffness matrices.

Lemma 4.4. *Suppose \mathbb{K}_K and \mathbb{D}_K are of SPD-type and \mathbb{D}_K satisfies ANAC. If \mathbf{b} has nonpositive divergence, then A_{ii} and M_{ii} are both strictly positive. If \mathbf{b} has strictly positive divergence, then $A_{ii} > 0$ if*

$$\tau_K > -\frac{\varphi_i}{\mathbf{b} \cdot \nabla \varphi_i} \quad (79)$$

and $M_{ii} > 0$ if

$$\tau_K < \frac{4|K|}{(d+1)(d+2)} \left(\int_K (\nabla \cdot \mathbf{b}) \varphi_i^2 d\mathbf{x} \right)^{-1}. \quad (80)$$

Proof. We consider a patch of elements Ω_i that share a vertex \mathbf{a}_i . Recall the definition of A_{ii} we have

$$A_{ii} = \sum_{K \in \Omega_i} \int_K \varphi_i \mathbf{b} \cdot \nabla \varphi_i + \tau_K (\mathbf{b} \cdot \nabla \varphi_i)^2 + \tau_K (\varepsilon \mathbb{D}_K \nabla \varphi_i) \cdot \nabla (\mathbf{b} \cdot \nabla \varphi_i) d\mathbf{x} + |K| (\nabla \varphi_i)^T \varepsilon \mathbb{D}_K \nabla \varphi_i \quad (81)$$

We first concentrate on the first two integrals and make use of τ_K in order to bound these integrals below by zero. Note that by (43) the first integral is nonnegative if \mathbf{b} has nonpositive divergence. Then

$$\int_K (\varphi_i (\mathbf{b} \cdot \nabla \varphi_i) + \tau_K (\mathbf{b} \cdot \nabla \varphi_i)^2) d\mathbf{x} \geq 0. \quad (82)$$

If \mathbf{b} has strictly positive divergence, then (82) holds under the condition (79). Indeed, (43) implies

$$\int_K \varphi_i (\mathbf{b} \cdot \nabla \varphi_i) d\mathbf{x} < 0 \quad (83)$$

and hence $\mathbf{b} \cdot \nabla \varphi_i < 0$ since $\varphi_i > 0$ on element $K \in \Omega_i$ and $\tau_K > 0$ for all $K \in \Omega$. By factoring out the convection term, the lower bound on τ_K given in equation (79) gives (82).

We now turn our attention to the third term in (81). Let λ_j and $\boldsymbol{\omega}_j$ be the quadrature weights and nodes, respectively on element $K \in \Omega_i$. Then

$$\int_K (\mathbb{D} \nabla \varphi_i) \cdot \nabla (\mathbf{b} \cdot \nabla \varphi_i) d\mathbf{x} \approx |K| \sum_{i=1}^m \lambda_j (\nabla (\mathbf{b}(\boldsymbol{\omega}_j) \cdot \nabla \varphi_i)^T \mathbb{D}(\boldsymbol{\omega}_j) \nabla \varphi_i) \quad (84)$$

$$= |K| (\nabla \varphi_i)^T \mathbb{K}_K (\nabla \varphi_i) \quad (85)$$

It follows from Lemma 4.2 that $A_{ii} > 0$.

On the other hand,

$$M_{ii} = \sum_{K \in \Omega_i} (\varphi_i, \varphi_i + \tau_K (\mathbf{b} \cdot \nabla \varphi_i))_{0,K} \quad (86)$$

$$= \sum_{K \in \Omega_i} \int_K (\varphi_i^2 + \tau_K \varphi_i (\mathbf{b} \cdot \nabla \varphi_i)) d\mathbf{x} \quad (87)$$

$$= \sum_{K \in \Omega_i} \left(\frac{2|K|}{(d+1)(d+2)} + \tau_K \int_K \varphi_i (\mathbf{b} \cdot \nabla \varphi_i) d\mathbf{x} \right). \quad (88)$$

As we saw previously, the integral is nonnegative if \mathbf{b} has nonpositive divergence. Otherwise, we apply the upper bound on τ_K given by (80). Hence, $M_{ii} > 0$. \square

Remark 4.2. To summarize the previous lemma, under the ANAC and SPD-type conditions, if \mathbf{b} is nonpositive, then A_{ii} and $M_{ii} > 0$. Otherwise, we require

$$-\frac{\varphi_i}{\mathbf{b} \cdot \nabla \varphi_i} < \tau_K < \frac{4|K|}{(d+1)(d+2)} \left(\int_K (\nabla \cdot \mathbf{b}) \varphi_i^2 d\mathbf{x} \right)^{-1}. \quad (89)$$

It is important to keep in mind that this estimate is only for those elements associated with A_{ii} on the interior of Ω . This estimate highlights the significant relationship between τ_K and the convection term.

Lemma 4.5. *If \mathbb{K}_K and \mathbb{D}_K are of SPD-type, satisfy ANAC, and if the following two conditions are met*

$$\frac{|K| \|\mathbf{b}\|_{\infty, K}^2}{\rho} \leq \cos(\check{\alpha}_{ij}) \quad (90)$$

and

$$\frac{2h_i^K \|\mathbf{b}\|_{\infty, K}}{\rho \sqrt{(d+1)(d+2)}} \leq \cos(\check{\alpha}_{ij}), \quad (91)$$

where $\rho = \min\{\rho_{\min}(\mathbb{K}_K), \rho_{\min}(\varepsilon \mathbb{D}_K)\}$, then $A_{ij} \leq 0$, for $i \neq j$.

Proof. For the \mathbf{A} matrix, we have

$$A_{ij} = \sum_{K \in \Omega_i \cap \Omega_j} \int_K \varphi_i \mathbf{b} \cdot \nabla \varphi_j + \tau_K (\mathbf{b} \cdot \nabla \varphi_j) (\mathbf{b} \cdot \nabla \varphi_i) + \tau_K (\varepsilon \mathbb{D}_K \nabla \varphi_j) \cdot \nabla (\mathbf{b} \cdot \nabla \varphi_i) d\mathbf{x} \quad (92)$$

$$+ |K| (\nabla \varphi_i)^T \varepsilon \mathbb{D}_K \nabla \varphi_j \quad (93)$$

We investigate the three terms in the integral of A_{ij} . The first integral can be simplified using Cauchy-Schwarz and Holder's inequalities along with (42),

$$\int_K \varphi_i (\mathbf{b} \cdot \nabla \varphi_j) d\mathbf{x} \leq \sqrt{\frac{|K|}{(d+1)(d+2)}} \|\mathbf{b}\|_{\infty, K} \|\nabla \varphi_i\|_{2, K} \quad (94)$$

$$= \sqrt{\frac{2}{(d+1)(d+2)}} \left(\frac{|K| \|\mathbf{b}\|_{\infty, K}}{h_i^K} \right). \quad (95)$$

For the second term, we again use Cauchy-Schwarz and Holder's inequality and have the following bound on the convection integral

$$\int_K (\mathbf{b} \cdot \nabla \varphi_i) (\mathbf{b} \cdot \nabla \varphi_j) d\mathbf{x} \leq \|\mathbf{b}\|_{\infty, K}^2 \frac{|K|}{h_i^K h_j^K}. \quad (96)$$

We have

$$A_{ij} \leq \sum_{K \in \Omega_i \cap \Omega_j} \left(\frac{\sqrt{2}|K|}{h_j^K \sqrt{(d+1)(d+2)}} \|\mathbf{b}\|_{\infty, K} + \tau_K \|\mathbf{b}\|_{\infty, K}^2 \frac{|K|}{h_i^K h_j^K} - \tau_K \frac{\cos(\check{\alpha}_{ij}^K)}{\check{h}_i^K \check{h}_j^K} - |K| \frac{\cos(\tilde{\alpha}_{ij}^K)}{\tilde{h}_i^K \tilde{h}_j^K} \right) \quad (97)$$

$$\leq \sum_{K \in \Omega_i \cap \Omega_j} \frac{|K| \|\mathbf{b}\|_{\infty, K}}{h_j^K} \left(\frac{\sqrt{2}}{\sqrt{(d+1)(d+2)}} + \frac{\tau_K \|\mathbf{b}\|_{\infty, K}}{h_i^K} \right) \quad (98)$$

$$- \frac{1}{h_i^K h_j^K} (\tau_K \cos(\check{\alpha}_{ij}^K) \rho_{\min}(\mathbb{K}_K) + |K| \cos(\tilde{\alpha}_{ij}^K) \rho_{\min}(\varepsilon \mathbb{D}_K)) \quad (99)$$

$$\leq \sum_{K \in \Omega_i \cap \Omega_j} \frac{|K| \|\mathbf{b}\|_{\infty, K}}{h_j^K} \left(\frac{\sqrt{2}}{\sqrt{(d+1)(d+2)}} + \frac{\tau_K \|\mathbf{b}\|_{\infty, K}}{h_i^K} \right) \quad (100)$$

$$- \frac{\min\{\rho_{\min}(\mathbb{K}_K), \rho_{\min}(\varepsilon \mathbb{D}_K)\}}{h_i^K h_j^K} (\tau_K \cos(\check{\alpha}_{ij}) + |K| \cos(\tilde{\alpha}_{ij})) \quad (101)$$

By (90) and (91), $A_{ij} \leq 0$. □

Lemma 4.6. *If*

$$\int_K \varphi_j (\mathbf{b} \cdot \nabla \varphi_i) d\mathbf{x} \geq 0 \quad (102)$$

or

$$\tau_K \leq - \frac{|K|}{(d+1)(d+2)} \left(\int_K \varphi_j (\mathbf{b} \cdot \nabla \varphi_i) d\mathbf{x} \right)^{-1}, \quad (103)$$

then $M_{ij} \geq 0$.

Proof. This is immediate based on the definition of M_{ij} and (21). \square

Combining the previous two lemmas, we have the following result.

Lemma 4.7. *Let \mathbb{K}_K and \mathbb{D}_K be of SPD-type, satisfy ANAC, and (90) and (91) be satisfied. The following nonnegative condition*

$$M_{ij} - \Delta t(1 - \theta)A_{ij} \geq 0 \quad (104)$$

holds for the off-diagonal entries if the convection integral is nonnegative or τ_K satisfies (103).

4.3 Temporal estimates

In this section we derive upper and lower bounds on the fixed time step Δt so that DMP is satisfied.

Lemma 4.8. *Suppose Δt satisfies*

$$\Delta t \geq -\frac{1}{\theta\sqrt{(d+1)(d+2)}} \max_{K \in \mathcal{T}_h} \max_{\substack{i,j=1,\dots,d+1 \\ i \neq j}} \left(\frac{|K|h_j^K \left(h_i^K + 2\tau_K \sqrt{(d+1)(d+2)} \|\mathbf{b}\|_{\infty,K} \right)}{2|K|h_i^K \|\mathbf{b}\|_{\infty,K} + \tau_K h_i^K \|\mathbf{b}\|_{\infty,K}^2 - \rho(\tau_K \cos(\tilde{\alpha}_{ij}) + |K| \cos(\tilde{\alpha}_{ij}))} \right), \quad (105)$$

where $\rho = \min\{\rho_{\min}(\mathbb{K}_K), \rho_{\min}(\varepsilon\mathbb{D}_K)\}$. Suppose also that \mathbb{K}_K and \mathbb{D}_K are of SPD-type, satisfy ANAC, and satisfy (90) and (91) (without equality). If, for each element K , \mathbf{b} has nonpositive divergence on or τ_K satisfies (89), then \mathbf{A} is an M -matrix.

Proof. From Lemma 4.4, the diagonal entries of $\mathbf{M} + \theta\Delta t\mathbf{A}$ is strictly positive. We show

$$M_{ij} + \theta\Delta tA_{ij} \leq 0, \quad \forall i \neq j, i = 1, \dots, N_{vi}, j = 1, \dots, N_v, \quad (106)$$

since this is equivalent to showing that $M + \theta\Delta tA$ is a Z -matrix and an M -matrix is a Z -matrix that is inverse positive.

For the \mathbf{M} matrix, we have

$$M_{ij} = \sum_{K \in \Omega_i \cap \Omega_j} \left(\frac{|K|}{(d+1)(d+2)} + \tau_K \int_K \varphi_j(\mathbf{b} \cdot \nabla \varphi_i) d\mathbf{x} \right) \quad (107)$$

The second integral term can be treated similar as (95). Now, we obtain the upper bound for M_{ij} ,

$$M_{ij} \leq \sum_{K \in \Omega_i \cap \Omega_j} \frac{|K|}{h_i^K [(d+1)(d+2)]^{3/2}} \left(h_i^K \sqrt{(d+1)(d+2)} + \tau_K \sqrt{2(d+1)(d+2)} \|\mathbf{b}\|_{\infty,K} \right). \quad (108)$$

Recall we have the following bound on A_{ij}

$$\begin{aligned} A_{ij} &\leq \sum_{K \in \Omega_i \cap \Omega_j} \frac{|K| \|\mathbf{b}\|_{\infty,K}}{h_j^K} \left(\frac{2}{\sqrt{(d+1)(d+2)}} + \frac{\tau_K \|\mathbf{b}\|_{\infty,K}}{h_i^K} \right) - \frac{\rho}{h_i^K h_j^K} (\tau_K \cos(\tilde{\alpha}_{ij}) + |K| \cos(\tilde{\alpha}_{ij})) \\ &= \sum_{K \in \Omega_i \cap \Omega_j} \frac{1}{h_i^K h_j^K \sqrt{(d+1)(d+2)}} \left(2h_i^K h_j^K |K| \|\mathbf{b}\|_{\infty,K} + h_j^K |K| \tau_K \sqrt{(d+1)(d+2)} \|\mathbf{b}\|_{\infty,K}^2 \right. \\ &\quad \left. - \rho \sqrt{(d+1)(d+2)} (\tau_K \cos(\tilde{\alpha}_{ij}) + |K| \cos(\tilde{\alpha}_{ij})) \right) \end{aligned} \quad (109)$$

Thus, $\tilde{\mathbf{A}}$ in (33) is a Z -matrix using the assumption on Δt .

By (33), we can write

$$\tilde{\mathbf{A}} = \begin{bmatrix} M_{11} + \theta\Delta t A_{11} & M_{12} + \theta\Delta t A_{12} \\ 0 & I_{N_v - N_{v_i}} \end{bmatrix}.$$

Since $\tilde{\mathbf{A}}$ is a Z -matrix, the block $M_{11} + \theta\Delta t A_{11}$ is also a Z -matrix. First, we show M_{11} is positive-definite. Let $\mathbf{v} = (v_1, v_2, \dots, v_{N_{v_i}})$ be a nonzero vector in $\mathbb{R}^{N_{v_i}}$ and write $v^h = \sum_{j=1}^{N_{v_i}} v_j \varphi_j \in U_h^0$. Using the assumption on the divergence of \mathbf{b} being either nonnegative or τ_K satisfying (89), $\mathbf{v}^T M_{11} \mathbf{v} > 0$ and $\mathbf{v}^T A_{11} \mathbf{v} > 0$ (this is a similar calculation as shown in Lemma 4.4). Therefore, $M_{11} + \theta\Delta t A_{11}$ is an M -matrix. We have

$$\tilde{\mathbf{A}}^{-1} = \begin{bmatrix} (M_{11} + \theta\Delta t A_{11})^{-1} & -(M_{11} + \theta\Delta t A_{11})^{-1}(M_{12} + \theta\Delta t A_{12}) \\ 0_{N_v} & I_{N_v - N_{v_i}} \end{bmatrix}, \quad (110)$$

which implies $\tilde{\mathbf{A}}$ is an M -matrix since $\tilde{\mathbf{A}}^{-1} \geq 0$ (note that $M_{12} + \theta\Delta t A_{12} \leq 0$). \square

Lemma 4.9. (104) holds along the diagonal entries if the mesh generated by \mathbb{D}_K and \mathbb{K}_K satisfy ANAC and are of SPD-type, and Δt satisfies the bound

$$\Delta t \leq \frac{1}{(1-\theta)(d+1)(d+2)} \min_{K \in \mathcal{T}_h} \min_{i,j=1,\dots,d+1} \frac{(\tilde{h}_i^K \check{h}_i^K)^2 (\tau_K (d+1)(d+2) \varphi_i(\mathbf{b} \cdot \nabla \varphi_i) + 2)}{|K|(\check{h}_i^K)^2 + (\tilde{h}_i^K \check{h}_i^K)^2 (\varphi_i(\mathbf{b} \cdot \nabla \varphi_i) + \tau_K (\mathbf{b} \cdot \nabla \varphi_i)^2) + \tau_K (\tilde{h}_i^K)^2} \quad (111)$$

Proof. From (88) and (81), along with (54), it's clear that if (111) holds, then $M_{ii} - (1-\theta)A_{ii} \geq 0$. \square

4.4 Metric tensor for DMP

We now develop the metric tensor to control the mesh so that the numerical solution satisfies DMP. Assume the temporal estimates from the previous section. As mentioned in the proof of Theorem 3.1 of [26], $\tilde{\mathbf{A}}^{-1} \geq 0$ and $\tilde{\mathbf{A}}$ is an M -matrix. To see that $\tilde{\mathbf{A}}$ has nonnegative row sums, note that $\sum_j \varphi_j = 1$. Therefore, the solution to (32) satisfies

$$\max_{i=1,\dots,(N+1)N_v} (u_h)_i = \max \left\{ 0, \max_{i \in S(\mathbf{f}^+)} (u_h)_i \right\}, \quad (112)$$

where $S(\mathbf{f}^+)$ is the set of indices where f_i is nonnegative. Piecewise linear functions attain their maximum value at the vertices of element K . Hence, when $f(\mathbf{x}, t) \leq 0$, we have

$$\max_{n=0,\dots,N} \max_{\mathbf{x} \in \bar{\Omega}} u_h^n(\mathbf{x}) = \max \left\{ 0, \max_{n=0,\dots,N} \max_{\mathbf{x} \in \bar{\Omega}} u_h^n(\mathbf{x}), \max_{\mathbf{x} \in \bar{\Omega}} u_h^0(\mathbf{x}) \right\}, \quad (113)$$

where

$$u_h^n = \sum_{j=1}^{N_{v_i}} u_j^n \varphi_j(\mathbf{x}) + \sum_{j=N_{v_i}+1}^{N_v} u_j^n \varphi_j(\mathbf{x}), \quad n = 0, \dots, N. \quad (114)$$

Theorem 4.10. Suppose the two meshes generated by \mathbb{D}_K and \mathbb{K}_K satisfy ANAC, are of SPD-type, and satisfy the step size bounds (105) and (111). If \mathbf{b} has nonpositive divergence or τ_K satisfies (89), then the SUPG scheme satisfies DMP.

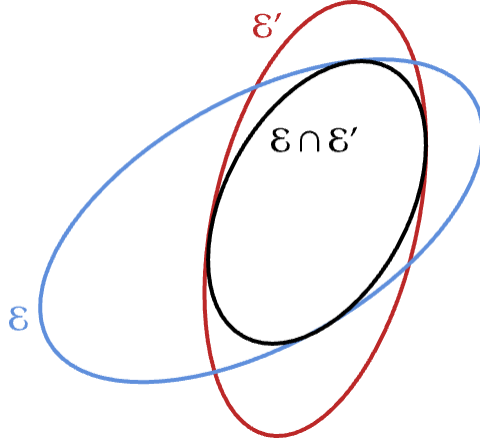


Figure 11: Geometric illustration of intersecting ellipses \mathcal{E} and \mathcal{E}' , resulting in $\mathcal{E} \cap \mathcal{E}'$.

Since two different metric tensors will be used on any given node, we follow [40] and taken into consideration for every time step, we use metric intersection in order to generate the anisotropic mesh. This is equivalent to finding the largest ellipsoid included in the intersection of the two ellipses \mathcal{E} and \mathcal{E}' , the geometric representations of symmetric, positive definite \mathcal{M} and \mathcal{M}' , respectively (see Figure 11). By our assumptions on \mathcal{M} and \mathcal{M}' , $\mathcal{N} = \mathcal{M}^{-1}\mathcal{M}'$ is diagonalizable by the similarity transform. Denote the shared normalized eigenvectors of \mathcal{M} and \mathcal{M}' by λ_1 and λ_2 and write

$$\mathcal{M}_{int} = \mathcal{M} \cap \mathcal{M}' = \Lambda^{-T} \text{diag}(\max\{\alpha_1, \beta_1\}, \max\{\alpha_2, \beta_2\}) \Lambda^{-1}. \quad (115)$$

Figure 12 shows the coordinate transformation of a typical element K to \tilde{K} and \check{K} .

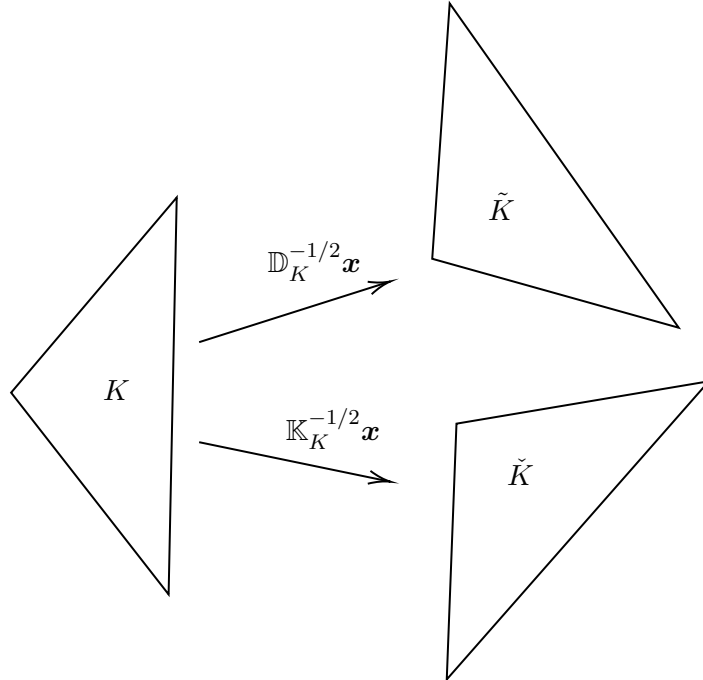


Figure 12: Coordinate transformation of a typical element K to \tilde{K} and \check{K} .

4.5 Numerical Results

In this section we present our numerical findings for using different metric tensors. We start with the metric tensors $\mathcal{M}_{DMP} = \theta \mathbb{D}^{-1}$ and $\mathcal{M}_{\mathbb{K}} = \theta' \mathbb{K}^{-1}$ and define the metric tensor $\mathcal{M}_{int} = \mathcal{M}_{DMP} \cap \mathcal{M}_{\mathbb{K}}$. We use the implicit Euler method in time for all computations (that is, $\theta = 1$) and compare the results with the classic Galerkin method with SUPG using fixed mesh (FM-SUPG).

Example 4.1. Consider the manufactured solution on the domain $\Omega_T = [0, 1]^2 \times [0.2, 0.3]$ to (1) given by

$$u(x, y, t) = (1 + \exp(C(x + y - t)))^{-1}, \quad C > 0 \quad (116)$$

with diffusion tensor defined by

$$\mathbb{D} = \begin{pmatrix} 50.5 & 49.5 \\ 49.5 & 50.5 \end{pmatrix}, \quad (117)$$

and time-dependent flow given by

$$\mathbf{b}(x, y, t) = (x + t, y + t). \quad (118)$$

In the computations, we have used $\varepsilon = 10^{-6}$ and $\Delta t = 10^{-2}$ for this example. Based on the maximum principle, the solution should satisfy $\min_{\Omega_T} u = 0$.

The diffusion tensor has eigenvalues $\lambda_1 = 100$ and $\lambda_2 = 1$, which indicates that the diffusion in horizontal direction is 100 times faster than that in the vertical direction. For the given flow in (118), the tensor \mathbb{K} defined in (50) is the same as \mathbb{D} . Therefore, the metric tensor \mathcal{M}_{DMP} is the same as $\mathcal{M}_{\mathbb{K}}$ for this example.

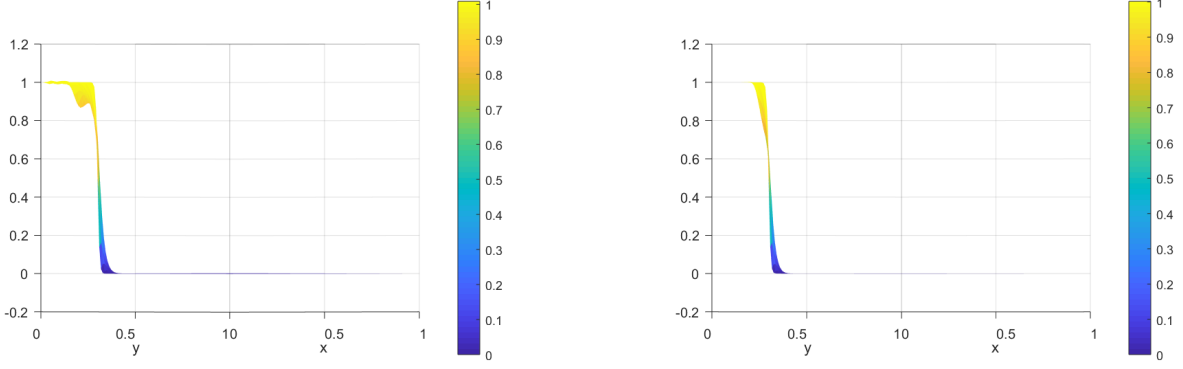
Table 5 presents the minimum values of the numerical solutions obtained from different meshes. As can be seen, the results from \mathcal{M}_{int} and \mathcal{M}_{DMP} are nearly identical. Even the results from the fixed mesh show satisfaction of DMP for the bottom shelf. However, the graph in Figure 13(a) shows significant artificial oscillation near the top shelf when using the fixed mesh approach. On the other hand, as shown in Figure 13(b), when using \mathcal{M}_{int} or \mathcal{M}_{DMP} , the artificial oscillation at the top shelf is essentially eliminated.

Table 5: Example 4.1. $\min_{\Omega_T} u$ with $\Delta t = 10^{-2}$.

N	\mathcal{M}_{int}	\mathcal{M}_{DMP}	Fixed mesh
16200	-4.4374e-05	-4.4373e-05	-2.8664e-07
24200	-3.1365e-06	-3.1367e-06	-2.2583e-08
34322	-1.5736e-07	-1.5735e-07	-1.1880e-09

Example 4.2. In this example, we consider the metric tensor $\mathcal{M}_{DMP+adapt}$ developed in [25] that is based on both DMP satisfaction as well as minimization of the H^1 -seminorm of the interpolation error. Correspondingly, our intersection metric tensor is $\mathcal{M}_{int+adapt} = \mathcal{M}_{DMP+adapt} \cap \mathcal{M}'$ where $\mathcal{M}' = \theta' \mathbb{K}^{-1}$. The anisotropic diffusion tensor is given by

$$\mathbb{D} = \begin{pmatrix} 1 & 1 \\ 1 & 3 \end{pmatrix} \quad (119)$$



(a): Fixed mesh

(b): \mathcal{M}_{int}

Figure 13: Example 4.1 – side view of solutions for a fixed mesh and \mathcal{M}_{int} with $N = 34322$, $\varepsilon = 10^{-6}$, and $\Delta t = 10^{-2}$.

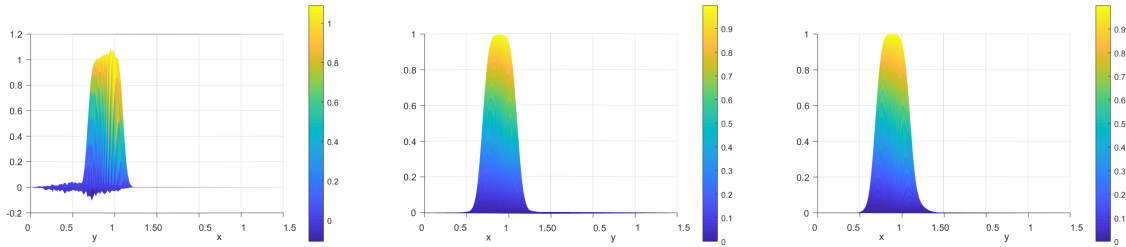
and the flow is given by

$$\mathbf{b}(x, y, t) = (x + y + t + 8, x + 3y + t + 16), \quad (120)$$

for $\Omega_T = [0, 1.5]^2 \times [0, 0.015]$. For the given \mathbf{b} and \mathbb{D} , we have

$$\mathbb{K} = \begin{pmatrix} 2 & 4 \\ 4 & 10 \end{pmatrix}. \quad (121)$$

We first use $N = 20,402$ elements in the mesh and compute the numerical solutions for $\varepsilon = 10^{-3}$ with time step size $\Delta t = 10^{-4}$. Figure 14 shows the side view of the solution using fixed mesh, $\mathcal{M}_{DMP+adapt}$ mesh and $\mathcal{M}_{int+adapt}$ mesh, respectively. As can be seen, $\mathcal{M}_{DMP+adapt}$ mesh and $\mathcal{M}_{int+adapt}$ mesh provide comparable results and both perform much better than the fixed mesh SUPG approach.



(a): Fixed mesh

(b): $\mathcal{M}_{DMP+adapt}$ (c): $\mathcal{M}_{int+adapt}$

Figure 14: Example 4.2 – side view with $\varepsilon = 10^{-3}$ for different metric tensors and $\Delta t = 10^{-4}$, $N = 20,402$.

To see the advantage of $\mathcal{M}_{DMP+adapt}$ mesh over $\mathcal{M}_{int+adapt}$ mesh, we compute the numerical solutions at different N values with larger time step $\Delta t = 10^{-3}$. The minimum values of the numerical solutions are summarized in Table 6. As can be seen, $\mathcal{M}_{int+adapt}$ provides the best results.

Table 6: Example 4.2. Results for $\mathcal{M}_{int+adapt}$, $\mathcal{M}_{DMP+adapt}$, and fixed mesh for varying N with $\varepsilon = 10^{-3}$ and $\Delta t = 10^{-3}$.

N	Fixed Mesh	$\mathcal{M}_{DMP+adapt}$	$\mathcal{M}_{int+adapt}$
3362	-2.4050e-01	-2.3330e-03	-3.6297e-03
13122	-1.6762e-01	-1.3796e-03	-6.8634e-04
29282	-1.0677e-01	-9.3509e-04	-1.8547e-04

5 Summary and Conclusions

In this paper, we have developed a moving mesh SUPG (MM-SUPG) method that integrates the moving mesh partial differential equation (MMPDE) methods with streamline upwind Petrov-Galerkin (SUPG) method for convection-diffusion problems. MM-SUPG method takes the advantage of the SUPG method to stabilize the numerical solution and the moving mesh method to adapt the mesh to improve the efficiency of the computation and accuracy of the solution. We considered convection-dominated problems where sharp layers exist in the solution. Both time-dependent and time-independent flows are investigated. And the method is designed to work with both isotropic and anisotropic diffusion tensors.

For isotropic diffusion case, our MM-SUPG method shows a $O(h^1)$ convergence rate in the H^1 -seminorm and $O(h^{1.5})$ convergence in the L^2 norm (see Figures 1 and 4). Even with moderately large N , we see in Figure 5 that oscillations can still be present when using moving mesh with standard Galerkin finite element method (MM-FEM). However, when using MM-SUPG method, the oscillations are significantly reduced and the solution is much smoother. The results in Examples 3.1 and 3.2 demonstrate the advantage of MM-SUPG over fixed mesh with SUPG (FM-SUPG) and moving mesh without SUPG (MM-FEM).

For anisotropic diffusion case, we have developed conditions for mesh and time step size so that the numerical solution satisfies the discrete maximum principle. Based on the diffusivity tensor \mathbb{D} and the flow vector \mathbf{b} , we have introduced a weighted diffusion tensor \mathbb{K} in (50) and developed a new metric tensor, \mathcal{M}_{int} in (115) to control the mesh. Numerical results in Examples 4.1 and 4.2 demonstrate that \mathcal{M}_{int} mesh provides better solution than other meshes in terms of DMP satisfaction.

In summary, the MM-SUPG method takes the advantage of both SUPG method and moving mesh method to provide a stable and accurate solution for convection-diffusion problems. Together with conditions for mesh and time step size, the MM-SUPG method can provide a solution that satisfies the discrete maximum principle, especially when the diffusion tensor is anisotropic.

References

- [1] Keith W Morton. *Revival: Numerical Solution Of Convection-Diffusion Problems (1996)*. CRC Press, Boca Raton, Florida, 2019.
- [2] Alexander N Brooks and Thomas JR Hughes. Streamline upwind/Petrov-Galerkin formulations for convection dominated flows with particular emphasis on the incompressible Navier-Stokes equations. *Computer methods in applied mechanics and engineering*, 32(1-3):199–259, 1982.
- [3] Yana Di, Hehu Xie, and Xiaobo Yin. Anisotropic meshes and stabilization parameter design of linear SUPG method for 2D convection-dominated convection–diffusion equations. *Journal of Scientific Computing*, 76(1):48–68, 2018.

- [4] Christoph Erath and Dirk Praetorius. Optimal adaptivity for the SUPG finite element method. *Computer Methods in Applied Mechanics and Engineering*, 353:308–327, 2019.
- [5] Marco Picasso and Virabouth Prachittham. An adaptive algorithm for the Crank–Nicolson scheme applied to a time-dependent convection–diffusion problem. *Journal of computational and applied mathematics*, 233(4):1139–1154, 2009.
- [6] Sashikumaar Ganesan and Shweta Srivastava. ALE-SUPG finite element method for convection–diffusion problems in time-dependent domains: Conservative form. *Applied Mathematics and Computation*, 303:128–145, 2017.
- [7] Thomas-Peter Fries, Hermann Matthies, et al. *A review of Petrov-Galerkin stabilization approaches and an extension to meshfree methods*. Citeseer, Technical University Braunschweig, 2004.
- [8] Leopoldo P Franca, Sergio L Frey, and Thomas JR Hughes. Stabilized finite element methods: I. application to the advective-diffusive model. *Computer Methods in Applied Mechanics and Engineering*, 95(2):253–276, 1992.
- [9] Tobias Gelhard, Gert Lube, Maxim A Olshanskii, and Jan-Hendrik Starcke. Stabilized finite element schemes with LBB-stable elements for incompressible flows. *Journal of computational and applied mathematics*, 177(2):243–267, 2005.
- [10] Matthias Augustin, Alfonso Caiazzo, André Fiebach, Jürgen Fuhrmann, Volker John, Alexander Linke, and Rudolf Umla. An assessment of discretizations for convection-dominated convection–diffusion equations. *Computer Methods in Applied Mechanics and Engineering*, 200(47-48):3395–3409, 2011.
- [11] Hoa Nguyen, Max Gunzburger, Lili Ju, and John Burkardt. Adaptive anisotropic meshing for steady convection-dominated problems. *Computer methods in applied mechanics and engineering*, 198(37-40):2964–2981, 2009.
- [12] Markus Bause and Peter Knabner. Uniform error analysis for Lagrange–Galerkin approximations of convection-dominated problems. *SIAM Journal on Numerical Analysis*, 39(6):1954–1984, 2002.
- [13] Markus Bause and Peter Knabner. On uniform convergence rates for Eulerian and Lagrangian finite element approximations of convection-dominated diffusion problems. *Calcolo*, 41(1):1–26, 2004.
- [14] Graham F Carey, M Anderson, B Carnes, and B Kirk. Some aspects of adaptive grid technology related to boundary and interior layers. *Journal of computational and applied mathematics*, 166(1):55–86, 2004.
- [15] PP Chinchapatnam, K Djidjeli, and PB Nair. Unsymmetric and symmetric meshless schemes for the unsteady convection–diffusion equation. *Computer methods in applied mechanics and engineering*, 195(19-22):2432–2453, 2006.
- [16] Volker John and Ellen Schmeier. Finite element methods for time-dependent convection–diffusion–reaction equations with small diffusion. *Computer methods in applied mechanics and engineering*, 198(3-4):475–494, 2008.

- [17] Volker John and Ellen Schmeier. On finite element methods for 3D time-dependent convection-diffusion-reaction equations with small diffusion. In *BAIL 2008-boundary and interior layers*, pages 173–181. Springer, Berlin, Heidelberg, 2009.
- [18] Volker John and Petr Knobloch. On spurious oscillations at layers diminishing (SOLD) methods for convection–diffusion equations: Part I—a review. *Computer methods in applied mechanics and engineering*, 196(17-20):2197–2215, 2007.
- [19] Yao Cheng, Yanjie Mei, and Hans-Goerg Roos. The local discontinuous Galerkin method on layer-adapted meshes for time-dependent singularly perturbed convection-diffusion problems. *arXiv preprint arXiv:2012.03560*, 2020.
- [20] Fajie Wang, Wen Chen, António Tadeu, and Carla G Correia. Singular boundary method for transient convection–diffusion problems with time-dependent fundamental solution. *International Journal of Heat and Mass Transfer*, 114:1126–1134, 2017.
- [21] Henry von Wahl, Thomas Richter, and Christoph Lehrenfeld. An unfitted Eulerian finite element method for the time-dependent stokes problem on moving domains. *arXiv preprint arXiv:2002.02352*, 2020.
- [22] Peter Hansbo, Mats G Larson, and Sara Zahedi. A cut finite element method for coupled bulk-surface problems on time-dependent domains. *Computer Methods in Applied Mechanics and Engineering*, 307:96–116, 2016.
- [23] Sara Zahedi. A space-time cut finite element method with quadrature in time. In *Geometrically Unfitted Finite Element Methods and Applications*, pages 281–306. Springer, Gewerbstrasse, Switzerland, 2017.
- [24] Santiago Badia, Francesc Verdugo, and Alberto F Martín. The aggregated unfitted finite element method for elliptic problems. *Computer Methods in Applied Mechanics and Engineering*, 336:533–553, 2018.
- [25] X. Li and W. Huang. An anisotropic mesh adaptation method for the finite element solution of heterogeneous anisotropic diffusion problems. *Journal of Computational Physics*, 229(21):8072–8094, 2010.
- [26] X. Li and W. Huang. Maximum principle for the finite element solution of time-dependent anisotropic diffusion problems. *Numerical Methods for Partial Differential Equations*, 29(6):1963–1985, 2013.
- [27] C. Lu, W. Huang, and J. Qiu. Maximum principle in linear finite element approximations of anisotropic diffusion–convection–reaction problems. *Numerische Mathematik*, 127(3):515–537, 2014.
- [28] Torsten Linß and Martin Stynes. Numerical methods on Shishkin meshes for linear convection–diffusion problems. *Computer methods in applied mechanics and engineering*, 190(28):3527–3542, 2001.
- [29] Ramon Codina. On stabilized finite element methods for linear systems of convection–diffusion–reaction equations. *Computer Methods in Applied Mechanics and Engineering*, 188(1-3):61–82, 2000.

- [30] Leopoldo P Franca and F Valentin. On an improved unusual stabilized finite element method for the advective–reactive–diffusive equation. *Computer Methods in Applied Mechanics and Engineering*, 190(13-14):1785–1800, 2000.
- [31] T Knopp, G Lube, and G Rapin. Stabilized finite element methods with shock capturing for advection–diffusion problems. *Computer methods in applied mechanics and engineering*, 191(27-28):2997–3013, 2002.
- [32] Gert Lube and Gerd Rapin. Residual-based stabilized higher-order FEM for advection-dominated problems. *Computer methods in applied mechanics and engineering*, 195(33-36):4124–4138, 2006.
- [33] Weizhang Huang and R. D. Russell. *Adaptive moving mesh methods*. Springer, New York, NY, 2011.
- [34] Avary Kolasinski and Weizhang Huang. A new functional for variational mesh generation and adaptation based on equidistribution and alignment conditions. *Computers & Mathematics with Applications*, 75(6):2044–2058, 2018.
- [35] Fei Zhang, Weizhang Huang, Xianping Li, and Shicheng Zhang. Moving mesh finite element simulation for phase-field modeling of brittle fracture and convergence of Newton’s iteration. *Journal of Computational Physics*, 356:127–149, 2018.
- [36] Shenglan Xie, Peng Zhu, and Xiaoshen Wang. Error analysis of weak galerkin finite element methods for time-dependent convection–diffusion equations. *Applied Numerical Mathematics*, 137:19–33, 2019.
- [37] L. C. Evans. Partial differential equations. *Graduate studies in mathematics*, 19(2), 1998.
- [38] J. H. Brandts, S. Korotov, and M. Krížek. The discrete maximum principle for linear simplicial finite element approximations of a reaction–diffusion problem. *Linear Algebra and its Applications*, 429(10):2344–2357, 2008.
- [39] G. Stoyan. On maximum principles for monotone matrices. *Linear algebra and its applications*, 78:147–161, 1986.
- [40] F. Alauzet and G. Olivier. Extension of metric-based anisotropic mesh adaptation to time-dependent problems involving moving geometries. in *49th AIAA Aerospace Sciences Meeting including the New Horizons Forum and Aerospace Exposition*, p. 896, 2011.